Astronomy & Astrophysics

One Star to Tag Them All (OSTTA)

I. Radial velocities and chemical abundances for 20 poorly studied open clusters[⋆]

R. Carrera[1], L. Casamiquela[2], A. Bragaglia[3], E. Carretta[3], J. Carbajo-Hijarrubia[4], C. Jordi[4], J. Alonso-Santiago[5], L. Balaguer-Nuñez[4], M. Baratella[6], V. D'Orazi[1], S. Lucatello[1], and C. Soubiran[2]

[1] INAF – Osservatorio Astronomico di Padova, vicolo Osservatorio 5, 35122, Padova, Italy
e-mail: `jimenez.carrera@inaf.it`
[2] Laboratoire d'Astrophysique de Bordeaux, Univ. Bordeaux, CNRS, B18N, allée Geoffroy Saint-Hilaire, 33615 Pessac, France
[3] INAF – Osservatorio di Astrofisica e Scienza dello Spazio di Bologna, via P. Gobetti 93/3, 40129 Bologna, Italy
[4] Institut de Ciències del Cosmos, Universitat de Barcelona (IEEC-UB), Martí i Franquès 1, 08028 Barcelona, Spain
[5] INAF – Osservatorio Astrofisico di Catania, via S. Sofia 78, 95123 Catania, Italy
[6] Leibniz-Institute for Astrophysics Potsdam (AIP), An der Sternwarte 16, 14482 Potsdam, Germany

ABSTRACT

Context. Open clusters are ideal laboratories to investigate a variety of astrophysical topics, from the properties of the Galactic disc to stellar evolution models. For this purpose, we need to know their chemical composition in detail. Unfortunately, the number of systems with chemical abundances determined from high resolution spectroscopy remains small.
Aims. Our aim is to increase the number of open clusters with radial velocities and chemical abundances determined from high resolution spectroscopy by sampling a few stars in clusters which had not been previously studied.
Methods. We obtained high resolution spectra with the FIbre-fed Echelle Spectrograph at Nordic Optical Telescope for 41 stars belonging to 20 open clusters. These stars have high astrometric membership probabilities determined from the *Gaia* second data release.
Results. We derived radial velocities for all the observed stars which were used to confirm their membership to the corresponding clusters. For Gulliver 37, we cannot be sure the observed star is a real member. We derived atmospheric parameters for the 32 stars considered to be real cluster members. We discarded five stars because they have very low gravity or their atmospheric parameters were not properly constrained due to low signal-to-noise ratio spectra. Therefore, detailed chemical abundances were determined for 28 stars belonging to 17 clusters. For most of them, this is the first chemical analysis available in the literature. Finally, we compared the clusters in our sample to a large population of well-studied clusters. The studied systems follow the trends, both chemical and kinematical, described by the majority of open clusters. It is worth mentioning that the three most metal-poor studied clusters (NGC 1027, NGC 1750, and Trumpler 2) are enhanced in Si, but not in the other α-elements studied (Mg, Ca, and Ti).

Key words. stars: abundances – stars: evolution – open clusters and associations: general

1. Introduction

The *Gaia* mission (Gaia Collaboration 2016) is providing unprecedented accurate positions (α and δ), proper motions (μ_α and μ_δ), and parallaxes (ϖ) for more than 1.8 billion stars (Gaia Collaboration 2021). Additionally, *Gaia* also measures magnitudes in three photometric bands, G, G_{BP}, and G_{RP}, providing a unique homogeneous database (Riello et al. 2021). Although in a more limited way *Gaia* also provides radial velocities, presently they are available for more than 7 million stars with $G_{RP} \leq 13$ mag (Katz et al. 2019) but their number will greatly increase with further data releases. The radial velocities are derived with the Radial Velocity Spectrometer (RVS), working at a resolution of $R = 11\,500$ and with small wavelength coverage centred at the infrared Ca II triplet, 845–872 nm (Cropper et al.

2018). Starting from *Gaia* data release 3[1], metallicities and some abundances will also be provided based on RVS data. While *Gaia* RVS will provide the largest spectroscopic data set ever, there are also many limitations, both in magnitude limits and in the precision reached. This is why different follow-up intermediate resolution (e.g. $R \sim 20\,000$) spectroscopic surveys have been organised in order to complement the *Gaia* capabilities, such as the *Gaia*-ESO Survey (GES, Gilmore et al. 2012; Randich et al. 2013), Apache Point Observatory Galactic Evolution Experiment (APOGEE, Majewski et al. 2017), GALactic Archaeology with HERMES (GALAH, De Silva et al. 2015), the forthcoming WHT Enhanced Area Velocity Explorer (WEAVE, Dalton et al. 2012), and 4-m Multi-Object Spectroscopic Telescope (4MOST, Guiglion et al. 2019) Galactic surveys. In total, they are going to measure radial velocities and chemical abundances for a few million stars. All together, they are leading to a revolution in our

---

[⋆] Full Tables B.2 and B.5 are only available at the CDS via anonymous ftp to `cdsarc.u-strasbg.fr` (`130.79.128.5`) or via `http://cdsarc.u-strasbg.fr/viz-bin/cat/J/A+A/663/A148`

[1] `https://www.cosmos.esa.int/web/gaia/dr3`

knowledge of the Milky Way as well as the surrounding galaxies including Galactic stellar clusters, of course.

Stellar clusters are groups of stars sharing the same general properties (age, distance, and initial chemical composition), and they are the ideal laboratories to test models of stellar and Galactic formation and evolution (Freeman & Bland-Hawthorn 2002). In particular, open clusters (OCs) can trace the disc properties and, when carefully selected, they can be used as observational constraints for stellar models from low to high mass, having ages from a few million years to about 10 Ga (e.g. Bragaglia & Tosi 2006; Cantat-Gaudin et al. 2020; Dias et al. 2021). *Gaia* high precision astrometry has allowed known open clusters to be confirmed or discarded (e.g. Cantat-Gaudin et al. 2019) and it has led to the discovery of hundreds of new ones (e.g. Castro-Ginard et al. 2018, 2019, 2020). A full characterisation and an accurate age derivation requires, however, one to know the metallicity and the full set of detailed abundances from all nucleosynthetic chains as well. For example, Bossini et al. (2019) determined ages for almost 270 OCs from *Gaia* photometry finding, on the other hand, degeneracies in almost all cases with metallicity.

Unfortunately, more than 90% of the about 3000 known OCs have never been studied using high resolution spectroscopy (e.g. Donati et al. 2015; Netopil et al. 2016, 2022; Magrini et al. 2017; Casamiquela et al. 2017; Smiljanic et al. 2018). This paucity is currently or will be partially filled by the named intermediate resolution surveys mentioned before. For example, APOGEE has observed stars belonging to about 130 OCs (Carrera et al. 2019; Donor 2020) and GES has also done so for those belonging to about 80 clusters (Bragaglia et al. 2022, Randich et al., in prep.). The key feature of these surveys resides in their ability to sample numerous clusters or in studying a significant fraction of the clusters members in all evolutionary phases, with tens to many hundred of stars observed in each cluster, as GES did. This is important to understand both the formation of the clusters (e.g. Jeffries et al. 2014; Mapelli et al. 2015) and the evolution of the stars' properties depending on rotation, activity, surface abundances, and key constraints to modern stellar evolutionary models (e.g. Bertelli Motta et al. 2018; Smiljanic et al. 2016). However, spectra of stars with the high metallicity typical of OCs are difficult to analyse at the intermediate resolution common to all large surveys because of line blending[2]. Only spectra with simultaneous high resolution ($R > 50\,000$) and wide spectral coverage can allow the measurements of the full set of the Fe-peak, CNO, α-elements, neutron-capture elements, etc., with the necessary high precision and accuracy.

The One Star to Tag Them All (OSTTA) project was designed to provide a high resolution spectroscopy follow-up of poorly studied open clusters. To do that, we have acquired spectra of a few objects per cluster in order to determine radial velocities and measure abundances of elements synthesised through all nucleosynthesis chains, therefore providing robust constraints to stellar evolutionary models and to the history of the Galactic disc. In this paper, we present the results for 41 stars in 20 open clusters.

The paper is organised as follows. The target selection, observations, and data reduction are discussed in Sect. 2. The radial velocity determination is described in Sect. 3. The chemical abundance determination is presented in Sect. 4. The results are discussed in the context of the majority of Galactic OCs in Sect. 5 including the orbit determination. Finally, the conclusions are summarised in Sect. 6.

2. Target selection, observations, and data reduction

The target selection was based on the astrometric membership probabilities determined by Cantat-Gaudin et al. (2019) for 1229 clusters taking advantage of the *Gaia* data release 2 (DR2) positions, proper motions, and parallaxes. These membership probabilities were determined by the unsupervised photometric membership assignment in stellar clusters (UPMASK) which is based on the κ-means clustering algorithm. We refer the reader to Cantat-Gaudin et al. (2019) for details on how the probabilities were assigned. We selected OCs for which composition based on spectroscopy was not available in the literature at the time of observations, and where at least a giant star brighter than $G \sim 14$ mag is among the most probable members. We also included stars in cluster UBC 54 which were first reported by Castro-Ginard et al. (2018) on the basis of *Gaia* DR2 positions, proper motions, and parallaxes. The list of sampled clusters together with their main features are listed in Table 1. The observed stars are listed in Table B.1 and their position in the colour-magnitude diagram of each cluster is shown in Fig. 1.

The observations were acquired during five nights, 12–16 December 2018, and complemented in another three nights, 18, 19, and 24 April 2019, with the FIbre-fed Echelle Spectrograph (FIES, Telting et al. 2014) in its highest spectral resolution, $R \sim 67\,000$. FIES is installed at the 2.5 m Nordic Optical Telescope (NOT) at the Observatorio del Roque de los Muchachos on the island of La Palma (Spain). The number of exposures for each star, together with the final signal-to-noise ratio (S/N), total exposure times, and dates of observations are summarised in Table B.1.

The bias subtraction, flat-field correction, order tracing, and extraction and wavelength calibration were performed by the FIEStool dedicated pipeline specifically developed for this instrument. After this, the sky and telluric subtraction were performed from the extracted and wavelength calibrated spectra still separated by orders. Then, we proceeded with the combination, normalisation, and merge of the different orders. All the steps were performed with the tools developed in the framework of the OCCASO[3] survey and described in detail by Carrera et al. (2022).

3. Radial velocities

Radial velocities, $v_{\rm rad}$, were measured as in Carrera et al. (2022). Briefly, the radial velocities of the 1D combined spectra were obtained by measuring the Doppler shifts of the spectral lines using the classical cross-correlation method (e.g Tonry & Davis 1979). To do that, the observed spectrum was cross-correlated against a template synthetic spectrum which better reproduces the observed one. The synthetic template for each star was selected from a synthetic grid using FERЯE[4] (Allende Prieto et al. 2006). We used the coarse *hnsc1*, *hnsc2*, and *hnsc3* grids described by Allende Prieto et al. (2018) with the following three dimensions: metallicity [M/H]; effective temperature, $T_{\rm eff}$; and surface gravity, $\log g$. All together, these grids cover spectral types between early M ($T_{\rm eff} = 3500$ K) and A ($T_{\rm eff} = 12\,000$ K). We refer the reader to Allende Prieto et al. (2018) for details about the ranges of the parameters covered by each grid. The grids, originally computed with an infinity resolution and

---

[2] Indeed, GES uses the high resolution UVES spectra for complete chemical characterisation.

[3] Open Clusters Chemical Abundances from Spanish Observatories survey (Casamiquela et al. 2016).

[4] Available at https://github.com/callendeprieto

Table 1. Parameters of the observed clusters.

Cluster	α_{ICRS} [deg]	δ_{ICRS} [deg]	ϖ [mas]	μ_α [mas yr^{-1}]	μ_δ [mas yr^{-1}]	Age [Ga]	A_V [mag]	Distance [pc]	X [pc]	Y [pc]	Z [pc]	R_{GC} [pc]
ASCC 23	95.047	46.71	1.59 ± 0.06	1.10 ± 0.18	−0.60 ± 0.18	0.23	0.34	630	−595	132	156	8936
Alessi 44	295.325	1.592	1.50 ± 0.22	0.46 ± 0.40	−2.32 ± 0.18	0.22	0.71	679	511	430	−121	7840
Alessi 62	284.026	21.597	1.59 ± 0.06	0.24 ± 0.16	−1.07 ± 0.18	0.69	0.78	650	388	512	98	7967
COIN−Gaia 2	15.06	55.409	0.79 ± 0.06	−4.46 ± 0.12	−1.93 ± 0.12	0.66	0.46	1204	−670	987	−155	9064
COIN−Gaia 6	28.101	58.636	0.28 ± 0.06	−2.35 ± 0.11	−0.49 ± 0.14	0.48	1.18	3259	−2126	2463	−187	10752
FSR 0951	95.573	14.65	0.55 ± 0.05	0.24 ± 0.12	0.07 ± 0.10	0.52	0.81	1757	−1684	−502	10	10036
Gulliver 37	292.077	25.347	0.64 ± 0.04	−0.77 ± 0.07	−3.74 ± 0.09	0.35	1.33	1438	727	1237	95	7712
King 23	110.459	−0.988	0.28 ± 0.06	−0.46 ± 0.08	−0.88 ± 0.09	1.95	0.17	3136	−2480	−1889	344	10983
NGC 581	23.339	60.659	0.37 ± 0.04	−1.38 ± 0.071	−0.50 ± 0.08	0.03	1.09	2502	−1541	1969	−78	10075
NGC 1027	40.677	61.616	0.88 ± 0.05	−1.75 ± 0.13	2.09 ± 0.17	0.19	1.01	1125	−805	785	30	9179
NGC 1647	71.481	19.079	1.67 ± 0.08	−1.06 ± 0.25	−1.50 ± 0.24	0.36	0.64	635	−608	−3	−183	8948
NGC 1750	75.926	23.695	1.36 ± 0.09	−0.96 ± 0.25	−2.37 ± 0.20	0.26	0.79	727	−715	10	−135	9055
NGC 2186	93.031	5.453	0.41 ± 0.05	0.41 ± 0.12	−1.99 ± 0.11	0.25	0.65	2251	−2052	−894	−243	10430
NGC 2281	102.091	41.06	1.90 ± 0.09	−2.95 ± 0.27	−8.32 ± 0.26	0.62	0.09	544	−518	46	158	8858
NGC 2345	107.075	−13.199	0.35 ± 0.05	−1.33 ± 0.10	1.34 ± 0.11	0.21	1.04	2663	−1829	−1933	−107	10351
NGC 2358	109.261	−17.143	1.06 ± 0.05	−1.35 ± 0.08	0.54 ± 0.09	0.66	0.02	908	−570	−705	−35	8938
NGC 7654	351.195	61.59	0.60 ± 0.05	−1.94 ± 0.15	−1.13 ± 0.15	0.15	1.85	1653	−641	1524	12	9109
Stock 1	294.146	25.163	2.45 ± 0.08	6.03 ± 0.31	0.30 ± 0.33	0.42	0.39	416	206	361	15	8141
Trumpler 2	39.232	55.905	1.43 ± 0.06	1.58 ± 0.19	−5.35 ± 0.17	0.11	0.86	710	−521	479	−49	8874
UBC 54	64.747	46.453	0.88 ± 0.05	3.32 ± 0.11	−3.76 ± 0.11	0.25	0.98	1105	−1006	452	−52	9357

Notes. Values obtained from Cantat-Gaudin et al. (2020) derived from *Gaia* DR2, except for proper motions and parallaxes, which have been recomputed using *Gaia* EDR3.
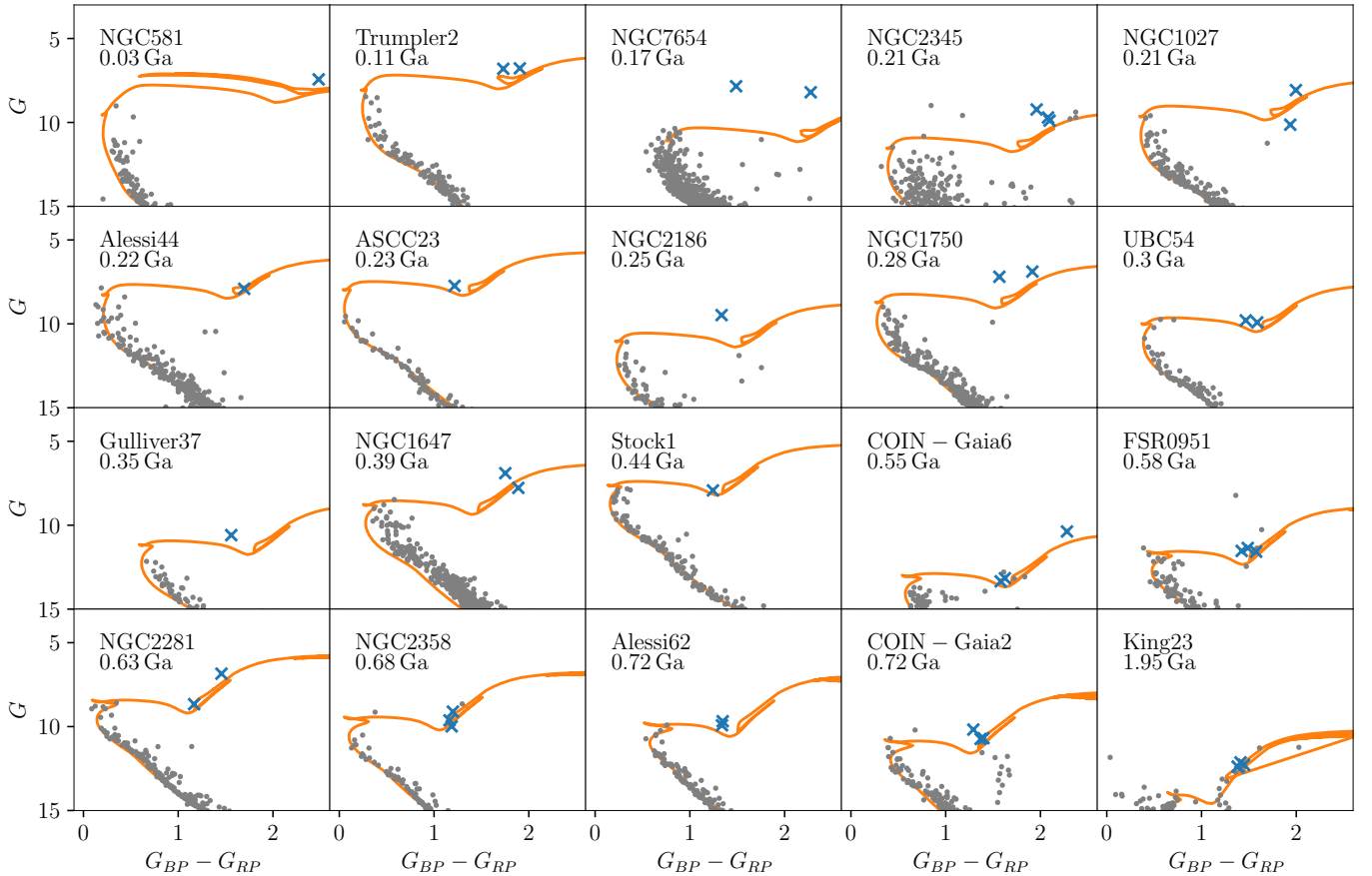
Fig. 1. *Gaia* DR2 colour-magnitude diagrams of the observed clusters, taking member stars from Cantat-Gaudin et al. (2020) (grey points). Blue crosses are spectroscopic targets sampled here. PARSEC isochrones (Marigo et al. 2017) at the metallicity computed in this paper were overplotted using distances, ages, and extinctions provided by Cantat-Gaudin et al. (2020). The clusters are ordered by increasing age. Ages are labelled in each panel.

0.45 km s^{-1} sampling equivalent to a resolution of 300 000, were smoothed to match the nominal resolution of FIES of 67 000.

Our procedure provides two independent determinations of the radial velocity uncertainties. The first one, v_{err}, is determined from the height of the cross-correlation peak. This value mainly depends on how well the template spectrum reproduces the observed one. The second one, $v_{scatter}$, is calculated as the velocity scatter of the individual measurements for each star, taking advantage of the fact that, in most cases, at least three individual exposures have been collected for each object. This value was obtained at the moment of combining the individual exposures by cross-matching each of them with the combined one, and therefore, it is model-independent. In principle, $v_{scatter}$ should be a better estimation of our internal precision than v_{err}, which systematically underestimates the radial velocity uncertainty. Moreover, large values of $v_{scatter}$ can be used as an indicator of binarity if individual exposures are adequately separated in time. Unfortunately, in our case, the individual exposures were often taken one after the other. From the detailed analysis presented by Carrera et al. (2022), the typical $v_{scatter}$ value for the instrumental configuration used in our case is 15.4 m s^{-1}.

The obtained radial velocities together with their uncertainties, both $v_{scatter}$ and v_{err}, and the number of individual exposures used in each case are listed in Table B.1. We used exactly the same tools as in Carrera et al. (2022), who have compared the larger OCCASO sample with different spectroscopic surveys available with the literature. They found that the obtained values are in agreement with the literature ones within the uncertainties involved in each case. We refer the reader to this paper for details. In this paper, we are going to concentrate on the individual comparison of our radial velocity with previous determinations available in the literature.

For those clusters where two or more stars were observed, the average radial velocity was derived following the equations described by Soubiran et al. (2018) and it is shown in Fig. 2. The small number of stars sampled in each cluster – for which there are three in the best case – prevented us from using statistical techniques, such as an iterative κ-σ clipping algorithm, in order to remove objects with discrepant radial velocities. Therefore, the membership probability of each star and the reliability of the average cluster radial velocity is discussed on the basis of the astrometric membership probabilities, p, determined from *Gaia* DR2 by Cantat-Gaudin et al. (2019, 2020); the radial velocities derived here; and other determinations available in the literature by Soubiran et al. (2018, S18) from *Gaia* DR2 radial velocities, Tarricq et al. (2021, T21) from a compilation including also *Gaia* DR2, and Mermilliod et al. (2008, M08) from their own observations.

A detailed discussion of each particular cluster can be found in Appendix A. The final values are listed in Table 2 together with other values available in the literature for comparison. A total of six stars were discarded as members by comparison with other objects in the same system for clusters Alessi 62, COIN-*Gaia* 2, FSR 0951, King 23, NGC 1027, and NGC 1750. Moreover, we considered another three stars as spectroscopic binaries in clusters Gulliver 37 and NGC 2345. Therefore, we removed Gulliver 37 from our sample since we cannot ensure that the only star sampled in this system is a real cluster member. These objects are properly flagged in Table B.1.

4. Chemical abundance determination

We derived atmospheric parameters and individual chemical abundances for all the stars considered as real cluster members
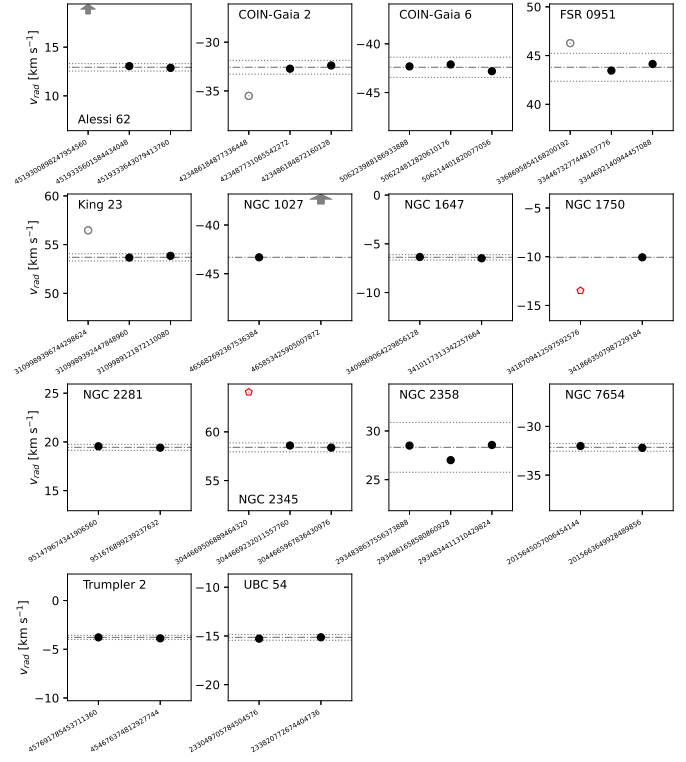
Fig. 2. Determination of the average radial velocity for each cluster with two or more stars sampled. Filled symbols mark stars considered real cluster members, while open symbols are the excluded objects. Red pentagons are the reported spectroscopic binaries. Arrows denote the objects outside the panels. Dot-dashed lines correspond to the average radial velocity for each cluster. Dotted lines show the $3 \times \sigma_{v_{rad}}$ level. We note that the error bars are smaller than the symbol size.

in the previous section. We excluded the eight stars considered as non-members or spectroscopic binaries in the previous section.

4.1. Method

The atmospheric parameters (T_{eff}, $\log g$, [M/H]) and individual chemical abundances were derived using the public spectroscopic software iSpec (Blanco-Cuaresma et al. 2014; Blanco-Cuaresma 2019). We made use of the synthetic spectral synthesis method in the 1D Local Thermodynamic Equilibrium (LTE) approach, with the radiative transfer code SPECTRUM (Gray & Corbally 1994) and the MARCS atmospheric models (Gustafsson et al. 2008). We used the latest version (the sixth one) of the line list from GES (Heiter et al. 2021). Atmospheric parameters and abundances were obtained in a two-step process, similarly as what was done in Casamiquela et al. (2020).

The atmospheric parameters T_{eff}, $\log g$, [M/H], and [α/M], as well as the microturbulence parameter v_{mic} were inferred for each spectrum using spectral synthesis fitting. The selection of lines from the master line list is the same as the one used in Casamiquela et al. (2017), which includes a sample of 330 atomic lines from different elements selected to be sensitive to the atmospheric parameters at the FIES resolution (67 000). In this step, we also used the wings of Hα and Hβ, as well as the Mg I *b* triplet lines, which are sensitive to the T_{eff}. As for the broadening parameters, we set the same strategy as in Casamiquela et al. (2020): only the spectral resolution was let free throughout the iterations, accounting for all broadening effects. We fixed the atmospheric parameters to the results of the previous step to

Table 2. Mean radial velocities obtained here for the observed clusters, together with other values available in the literature.

Cluster	$v_{\rm rad}$	$\sigma_{v_{\rm rad}}$	$e_{v_{\rm rad}}$[a]	N	$v_{\rm S18}$	$e_{v_{\rm S18}}$	$\sigma_{v_{\rm S18}}$	$N_{\rm S18}$	$v_{\rm T21}$	$e_{v_{\rm T21}}$	N_{T21}	$v_{\rm M08}$	$\sigma_{\rm M08}$	$N_{\rm M08}$
ASCC 23	−13.35		0.02	1	−13.29	1.49	3.65	6	−13.3	1.38	9			
Alessi 44	−9.58		1.11	1	−9.8	0.67	1.78	7	−10.68	12.95	9			
Alessi 62	12.93	0.13	0.09	2	13.28	0.2	0.68	12	13.28	0.21	10			
COIN-*Gaia* 2	−32.58	0.23	0.17	2					−34.55	2.41	3			
COIN-*Gaia* 6	−42.41	0.35	0.20	3					−47.26	3.75	3			
FSR 0951	43.80	0.48	0.34	2	45.53	0.55	1.24	5	45.01	2.04	5			
King 23	53.69	0.12	0.08	2	54.01	0.43	0.86	4	54.01	0.43	4			
NGC 581	−46.78		0.01	1	−45.33	0.32	0.0	1	−44.09	0.7	1	−44.2	0.12	2
NGC 1027	−43.32		0.02	1	−4.06	0.31		1	-36.57	10.83	6			
NGC 1647	−6.39	0.09	0.06	2	−6.69	0.21	0.86	16	−6.71	0.17	21	−7.02	0.22	2
NGC 1750	−10.06		0.01	1	−10.38	0.87	2.31	7	−7.45	6.64	13			
NGC 2186	20.82		0.02	1	21.98	0.26	0.0	1	21.71	4.01	3	20.15	0.19	1
NGC 2281	19.44	0.10	0.07	2	19.58	0.34	2.19	42	18.95	0.95	40	19.05	0.04	2
NGC 2345	58.41	0.15	0.11	2	60.94	2.0	4.89	6	63.27	2.43	6	59.19	0.36	4
NGC 2358	28.31	0.85	0.49	3	27.57	0.6	1.03	3	27.57	0.6	3			
NGC 7654	−32.15	0.13	0.09	2	−32.09	0.13	0.1	2	−32.18	0.27	2	−32.98	0.11	1
Stock 1	−19.60		0.24	1	−19.51	0.53	2.91	30	−19.52	0.55	29			
Trumpler 2	−3.78	0.07	0.05	2	−4.12	0.09	0.28	11	−3.97	1.14	12			
UBC 54	−15.15	0.10	0.07	2					−15.26	0.33	2			

Notes. [a]For those clusters with a single observed star, $e_{v_{\rm rad}}$ is the $v_{\rm scatter}$ of that object.
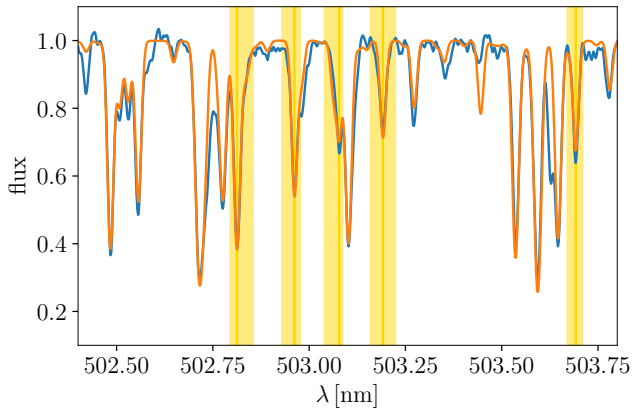

Fig. 3. Portion of the observed spectrum of the star *Gaia* EDR3 2934861658580860928 (blue) and the best synthetic fit (orange) obtained to constrain the atmospheric parameters. The line masks where the fit was performed are marked in yellow, and they correspond to five Fe I lines.

determine the absolute chemical abundances of individual lines, also using spectral synthesis fitting.

The spectral fitting was done by comparing the observed fluxes weighted by their uncertainties with a synthetic spectrum for the mask regions of the selected spectral features. The best fit was selected using a least-squares algorithm. The uncertainty in the atmospheric parameters was obtained from the χ^2 of the fit. Figure 3 shows an example of the observed spectrum for star *Gaia* Early data release 3 (EDR3) 2934861658580860928 of the cluster NGC 2358 with several selected features and the corresponding fits.

For the individual abundance determination, we used a custom line selection built in the same way as in Casamiquela et al. (2020) but performing with the spectra used in this study. In brief, it consisted in keeping the lines that give consistent abundances in all stars for elements with a high enough number of detected initial lines ($\gtrsim 10$). For the elements with few lines available, we kept the lines based on the flags provided by the GES line list group (LOGGFFLAG and SYNFLAG). Our final selection contained 209 lines from 17 chemical species.

4.2. Atmospheric parameters

The determined atmospheric parameters are listed in Table B.2 and represented in Kiel diagrams in Fig. 4. Most of the stars belong to the red clump or the red giant branch, but there are several stars which are probably red supergiants, particularly one star of NGC 7654 and another one of COIN-*Gaia* 6 with surface gravities close to zero. Since their spectra are very crowded with atomic and molecular lines, this makes their determination of atmospheric parameters and abundances more uncertain. The other two stars in COIN-*Gaia* 6 have low S/N spectra. Their spectra appeared very crowded, and the fits performed by our pipeline are not satisfactory. Finally, we also excluded the star observed in NGC 581 which was reported as an M supergiant in the literature by Keenan & McNeil (1989). We tried to derive the atmospheric parameters for this star, but the obtained fit was of a very poor quality. We excluded these suspected objects from our posterior analysis.

Several stars appear far from the predicted isochrone: the remaining star in NGC 7654 and the one in NGC 2186. For these stars, the synthetic fits were satisfactory, and our pipeline converged well. In these two cases, we also saw a shift from the isochrone in the colour-magnitude diagram (Fig. 1), thus probably the age of these clusters is not correct (see discussion about NGC 7654 in Appendix A).

Finally, there are several cases (NGC 1027, NGC 1750, and NGC 1647) for which stars appear far from the isochrone in the colour-magnitude diagrams, but not in the Kiel diagram. This thus indicates that there is probably an issue in the photometry, such as an unresolved companion or maybe the colour-magnitude diagrams are affected by differential reddening.
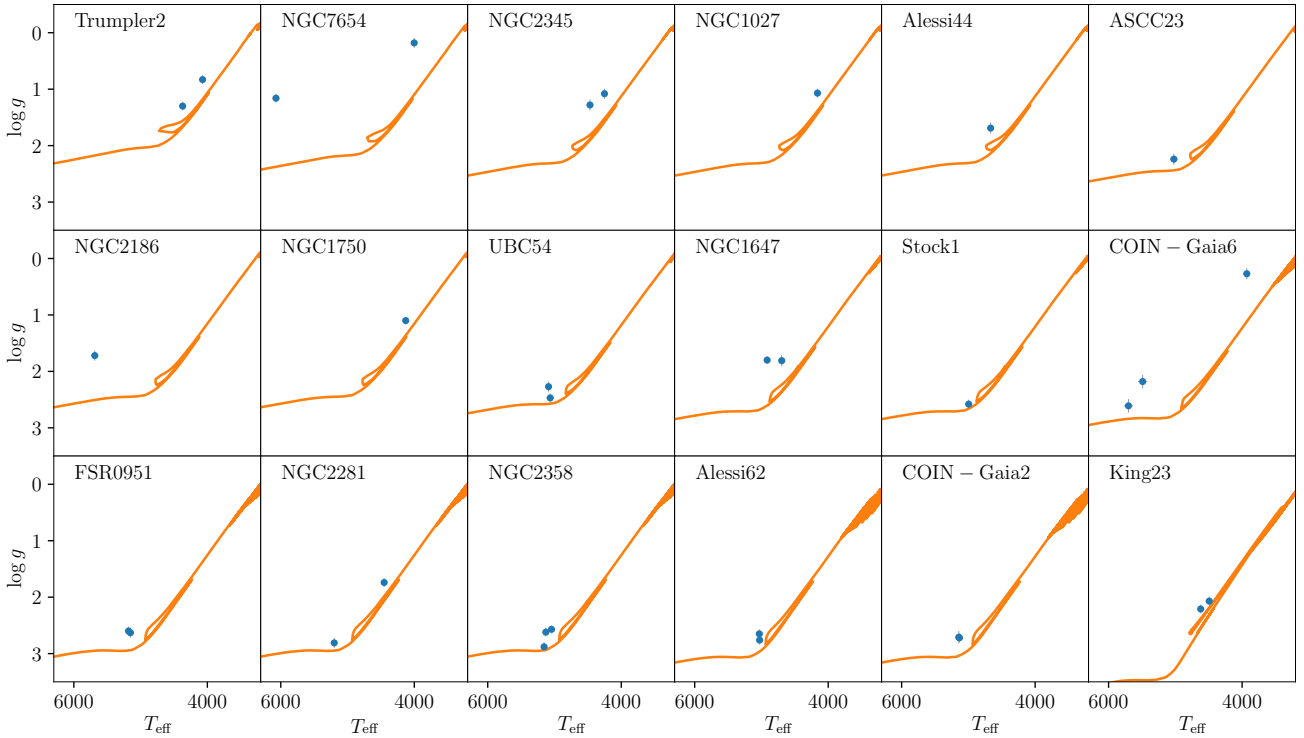
Fig. 4. Kiel diagram of the analysed stars. As in Fig. 1, the corresponding isochrones for the age of each cluster are overplotted as a reference.

NGC 2345 is the only cluster in our sample which has been properly studied before. The same three stars sampled here were studied by Reddy et al. (2016), Alonso-Santiago et al. (2019), and Holanda et al. (2019). One of them is a spectroscopic binary, as specified in Appendix A. The results obtained here and in the literature are summarised in Table B.2. In general, there is good agreement within the uncertainties for the two stars. The exception is the gravity for the coolest star (3044665967836430976) for which Reddy et al. (2016) report a significantly larger gravity. For the iron abundances, the values obtained here are higher by about 0.17 dex, which is about twice that for the involved uncertainties. This could be explained by the existence of a zero-point between these measurements, although all of them used a similar Fe abundance for the Sun.

Luck (2014) determined atmospheric parameters for one of the stars in NGC 7654 (2015663649928489856). The effective temperature (6114 K) and metallicity (−0.06 dex) are in agreement within the uncertainties with the values found here. The surface gravity determined by this author (1.63 dex) is slightly higher than the value found here. Unfortunately, Luck (2014) does not provide information about the uncertainties of his determinations. Additionally, Kovtyukh (2007) also determined the effective temperature for the star 2015663649928489856 in NGC 7654 (6268 ± 149 k), which again is in agreement with our value within the uncertainties. Additionally, the sampled star in Gulliver 37 has been recently analysed by Zhang et al. (2021). We excluded this object from our analysis because it was reported as a variable in the literature (Mermilliod et al. 2008). To our knowledge, these are the only determinations of atmospheric parameters available in the literature for the stars studied here.

4.3. Chemical abundances

We computed abundances for the following 17 chemical species: Na, Mg, Al, Si, Ca, Sc, Ti, V, Cr, Mn, Fe, Co, Ni, Y, Ba, Ce,

and Nd. We derived our own Solar abundances from the analysis of a Solar spectrum of the spectral library of the *Gaia* FGK benchmark stars (Blanco-Cuaresma et al. 2014), degraded to the FIES resolution. The determination of Solar abundances using the same analysis method allows one to partly take biases in the obtained [X/H] abundance values into account that could be caused by the performance of a particular method. The obtained solar abundances are listed in Table B.4.

Individual stellar abundances were computed as the median of the individual line abundances, and the median absolute deviation is assigned as an error. When a single line was measured for a particular element, the error assigned is that of the line fit (computed from the residuals of the fit). As an example, we plotted in Fig. 5 the Fe, Si, Mg, and Ni abundances for the sample of stars.

There exists a significant trend in most of the abundances with respect to the atmospheric parameters of the stars, except for Si. This behaviour is most probably caused by systematic effects from the analysis, and this has been thoroughly discussed in previous works (see an extensive discussion in Roederer et al. 2014). It can be caused for a variety of reasons, for example due to the fact that as temperature decreases lines can become more affected by blends, which are often not identified, and they can bias the abundance results. This bias can affect the various elements differently, as seen in Casamiquela et al. (2020), and it probably depends on the analysis method and line list used. A correction of such trends can be attempted by using empirical relations (e.g. Valenti & Fischer 2005), but it is usually difficult and risky because the underlying reasons are not always well understood. Moreover, to do so, a large number of stars with the same abundance and a wide coverage of the parameter space is needed, so we do not attempt to correct those trends in this study.

In general, the studied clusters have nearly solar metallicities, as expected for their ages. The clusters that have more than one observed star (Alessi 62, COIN-*Gaia* 2, FSR 0951, King 23,
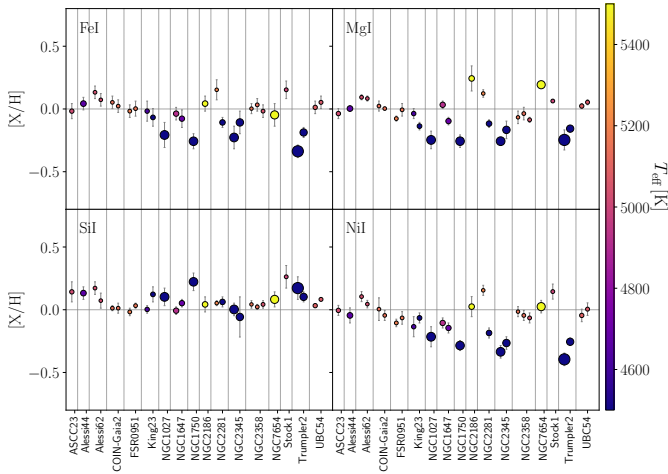
Fig. 5. Individual star abundances from Fe I, Mg I, Si I, and Ni I lines. Stars are coloured according to the effective temperature, and their size is proportional to the surface gravity (larger points represent lower surface gravities). Vertical lines separate stars from the different clusters.

NGC 1647, NGC 2281, NGC 2345, NGC 2358, Trumpler 2, and UBC 54) have good internal agreement in terms of chemical abundances. Trumpler 2 is probably the only case where we see discrepant abundances at the level of 0.1 dex among the two stars, remarkably in Ni and Fe, but not in Si and Mg. This can be explained by the difference in gravity among them of 0.5 dex, which, as has been explained previously, can cause small biases in the abundances of certain elements. Mean cluster abundances for all chemical species analysed are plotted in Fig. 6 and given in Table B.5.

The clusters Trumpler 2 and NGC 1750 are the most metal-poor clusters in our sample, with iron abundances [Fe/H] of -0.26 ± 0.12 and -0.26 ± 0.06 dex, respectively. This is surprising given their young age (110 and 280 Ma, respectively). Similar cases have been recently reported in the literature (e.g. Baratella et al. 2020; Zhang et al. 2021), where clusters with relatively young ages show large discrepancies when compared to chemical models, with metallicities that are too low for their Galactocentric positions. One of the hypotheses for this is the difficulty in deriving abundances for young stars due to their chromospheric activity and magnetic fields. A similar effect also explains the remarkable enhancement of Ba seen in our sample and in multiple works in the literature (e.g. Baratella et al. 2021). Alternatively, it could be that the lower Fe abundances obtained are partly explained by the previously mentioned trend of most elements with atmospheric parameters (see Fig. 5). Since the giant stars in younger clusters have smaller $T_{\rm eff}$ and $\log g$, our abundances for the elements that exhibit a trend with atmospheric parameters could display a zero-point which depends on age.

Almost all clusters in our sample exhibit a Na enhancement. Similar enhancements have been found in the literature for red giants in clusters. High-mass giant stars can present overabundances up to 0.2 dex (Smiljanic et al. 2016, 2018), which are attributed to the effects of internal mixing and can be described by some stellar evolutionary models as in Lagarde et al. (2012).

5. Observed clusters in the Galactic context

In this section, we investigate the properties of the studied clusters in comparison with the global kinematics and chemical trends observed in the Galactic disc.

5.1. Open clusters' kinematics

To check if the studied clusters follow the same kinematics as the majority of the OCs in the disc, we computed the line-of-sight velocity with respect to the Galactocentric standard of rest ($v_{\rm GSR}$) and with respect to the regional standard of rest[5] ($v_{\rm RSR}$), assuming $(U_\odot, V_\odot, W_\odot) = (11.10, 12.24, 7.25)$ km s^{-1} from Schönrich et al. (2010) and $R_0 = 8.34$ kpc from Reid et al. (2014). For the circular velocity around the Galactic centre, Θ_0 was adopted as 240 km s^{-1} from Reid et al. (2014), and Θ_R was computed from the *MW2014* Galactic potential (Bovy 2015). This is axisymmetric and composed of a spherical bulge, a Miyamoto-Nagai disc, and a halo with a Navarro-French-White (NFW) profile (Navarro et al. 1997).

The obtained radial velocities were combined with the mean proper motions from *Gaia* EDR3 and distances from Cantat-Gaudin et al. (2020) to derive full spatial velocities with respect to the Galactocentric standard of rest (V_R, V_ϕ, V_z) and to the regional standard of rest (U_s, V_s, W_s), being $U_s = -V_R$, $V_s = V_\phi - \Theta_R$ and $W_s = V_z$. The results are listed in Table 3. For those clusters without $\sigma_{v_{\rm rad}}$ values, we assumed $\sigma_{v_{\rm rad}} = 1$ km s^{-1}: ASCC 23, Alessi 44, NGC 581, NGC 1027, NGC 1750, NGC 2186, and Stock 1. The uncertainties were estimated with a Monte Carlo experiment with 10^5 realisations, taking the uncertainties in radial velocities and distances of the clusters into account. The clusters show $v_{\rm RSR}$ values typical of the thin disc kinematics (i.e. from -25 to $+20$ km s^{-1}), and therefore they are typical of the thin disc kinematics (Binney & Tremaine 2008).

Figure 7 shows the projection on the Galactic plane of the position and velocity with respect to the regional standard of rest of the clusters in our sample. Although the projection of the velocity of Alessi 44 and Stock 1 are similar (group A in Fig. 7), their vertical components, W_s, are not in agreement. The same happens for the pair COIN-*Gaia* 2 and NGC 1027 (group B). The trio ASCC 23, NGC 1647, and NGC 1750 (group C) share similar components for U_s, V_s and W_s, and their ages range from 0.23 to 0.39 Ga.

5.2. Open clusters' orbits

The orbits of the OCs in our sample were integrated using the python *galpy* package (Bovy 2015) using the same *MW2014* Galactic potential described above, but we added two non-axisymmetric components: a bar and spiral arms. The bar was characterised with a Ferrers potential (Ferrers 1877) with $n = 2$; the semi-major, middle, and minor axes are fixed to 3, 0.35, and 0.2375 kpc, respectively. The bar mass is $10^{10} M_\odot$ (Romero-Gómez et al. 2015) and a constant pattern speed was fixed to $\Omega = 42$ km s^{-1} kpc^{-1} (Bovy et al. 2019), which puts co-rotation at $R = 5.6$ kpc and the outer Lindblad resonance at $R = 9$ kpc. The angular orientation of the bar with respect to the Sun-Galactic centre line is 20° (Romero-Gómez et al. 2011, and references therein). For the spiral arms, we took the potential from Cox & Gómez (2002), assuming two arms with an amplitude of 0.4 and a pattern speed of $\Omega = 21$ km s^{-1} kpc^{-1} (e.g. Antoja et al. 2011), which puts co-rotation at $R = 10.6$ kpc.

We integrated the orbit backwards in time during the age of the cluster with a step of 2 Ma. The uncertainties of the derived orbital parameters were estimated using Monte Carlo sampling, assuming Gaussian distributions for radial velocities, proper motions, distances, and their respective uncertainties. The derived orbital parameters and their uncertainties are listed in
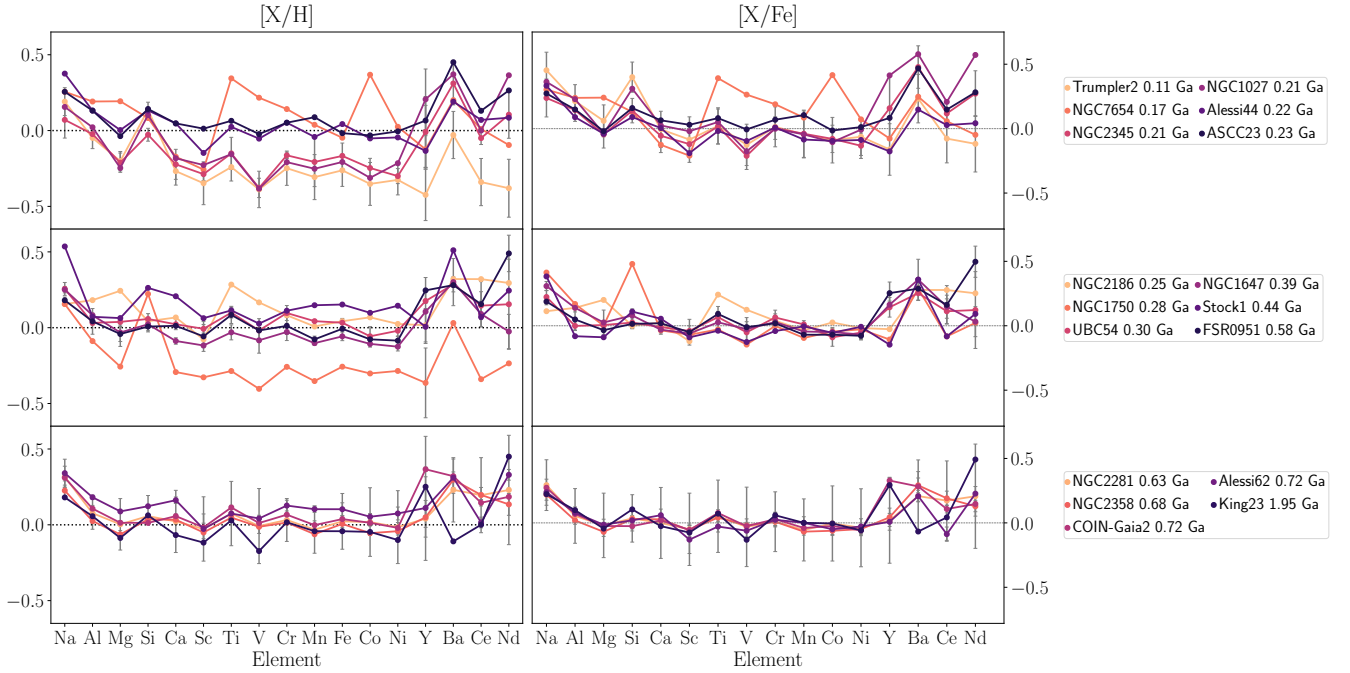

Fig. 6. Mean cluster chemical abundances. Clusters are sorted by age in the panels increasing downwards, and in each panel from yellow (younger) to black (older).

Table 3. Values of v_{GSR}, v_{RSR}, (U_s, V_s, W_s), and V_ϕ determined for each cluster.

Cluster	v_{GSR} [km s^{-1}]	v_{RSR} [km s^{-1}]	U_s [km s^{-1}]	V_s [km s^{-1}]	W_s [km s^{-1}]	V_ϕ [km s^{-1}]
ASCC 23	31.0 ± 1.0	-15.9 ± 1.0	19.9 ± 1.0	8.3 ± 0.5	5.9 ± 0.6	246.8 ± 0.6
Alessi 44	157.4 ± 1.0	-5.4 ± 1.4	-6.3 ± 1.4	-0.6 ± 1.0	4.0 ± 1.1	241.0 ± 1.0
Alessi 62	219.3 ± 0.1	20.5 ± 0.9	4.3 ± 1.5	20.6 ± 0.4	7.0 ± 0.6	261.8 ± 0.4
COIN$-Gaia$ 2	167.2 ± 0.2	-12.5 ± 1.6	24.5 ± 0.6	4.4 ± 1.9	-1.3 ± 1.3	242.4 ± 1.7
COIN$-Gaia$ 6	140.5 ± 0.3	4.0 ± 3.5	7.6 ± 2.3	17.0 ± 3.5	-6.4 ± 2.0	250.1 ± 2.8
FSR 0951	-38.9 ± 0.5	16.9 ± 1.1	-18.7 ± 1.1	5.5 ± 1.1	9.2 ± 0.8	240.6 ± 1.0
King 23	-106.2 ± 0.1	0.2 ± 2.8	9.7 ± 2.9	-18.4 ± 0.9	0.9 ± 1.6	214.1 ± 1.3
NGC 1027	124.9 ± 1.0	-25.7 ± 1.8	31.4 ± 1.3	-2.6 ± 1.7	11.9 ± 1.2	235.1 ± 1.5
NGC 1647	-20.6 ± 0.1	-19.3 ± 0.1	18.9 ± 0.3	12.2 ± 0.7	3.8 ± 0.8	250.6 ± 0.7
NGC 1750	-18.5 ± 1.0	-21.8 ± 1.0	22.1 ± 1.0	9.3 ± 0.7	1.5 ± 1.0	247.4 ± 0.8
NGC 2186	-90.3 ± 1.0	-15.9 ± 1.9	20.5 ± 2.4	-9.8 ± 1.8	-1.4 ± 1.2	224.3 ± 2.3
NGC 2281	32.3 ± 0.1	13.3 ± 0.2	-14.6 ± 0.7	-1.6 ± 1.6	-1.6 ± 1.5	237.1 ± 1.7
NGC 2345	-132.6 ± 0.2	4.2 ± 3.0	-2.6 ± 2.1	-3.5 ± 2.6	-2.3 ± 1.4	230.8 ± 2.1
NGC 2358	-175.0 ± 0.9	-2.2 ± 1.5	8.2 ± 1.5	-4.9 ± 0.8	2.1 ± 0.5	233.6 ± 0.7
NGC 581	144.7 ± 1.0	-8.2 ± 3.2	7.0 ± 2.7	-4.6 ± 1.9	-1.2 ± 1.2	230.5 ± 1.5
NGC 7654	196.1 ± 0.1	-4.5 ± 2.1	0.3 ± 2.2	-5.2 ± 1.3	2.9 ± 1.3	232.7 ± 1.1
Stock 1	205.1 ± 1.0	-9.0 ± 1.1	-14.6 ± 1.8	-2.5 ± 1.0	-3.6 ± 1.2	238.3 ± 1.0
Trumpler 2	157.9 ± 0.1	6.5 ± 1.0	-6.6 ± 1.9	1.5 ± 1.0	-7.2 ± 1.5	240.1 ± 1.1
UBC 54	77.7 ± 0.1	-8.8 ± 1.0	3.3 ± 1.9	-14.9 ± 2.3	5.7 ± 1.3	222.3 ± 2.6

Table B.6. Figure 8 shows an example of the orbits obtained for Stock 1 (left) and King 23 (right).

It is far from the scope of this paper to perform a detailed analysis of the derived orbits due to the fact that the average radial velocities of several clusters have to be confirmed with the observations of more members. However, it is interesting to compare the derived orbital properties to the majority of the OC sample. To do that, we used the values derived by Tarricq et al. (2021) who integrated the orbits using a similar procedure as the one used here for a sample of more than 1300 clusters.

In the top panel of Fig. 9, we plotted the run of maximum height above the plane z_{max} as a function of age for our clusters overplotted to the Tarricq et al. (2021) high-quality sample. One can see the signs of vertical heating (Spitzer & Schwarzschild 1951; Jenkins & Binney 1990) and that our clusters follow the general trend.

In the case of eccentricity, e (bottom panel of Fig. 9), the studied clusters tend to be among the systems with the largest eccentricities for their given ages, and even above them, as is the case of the oldest ones: Alessi 62 and King 23. However,
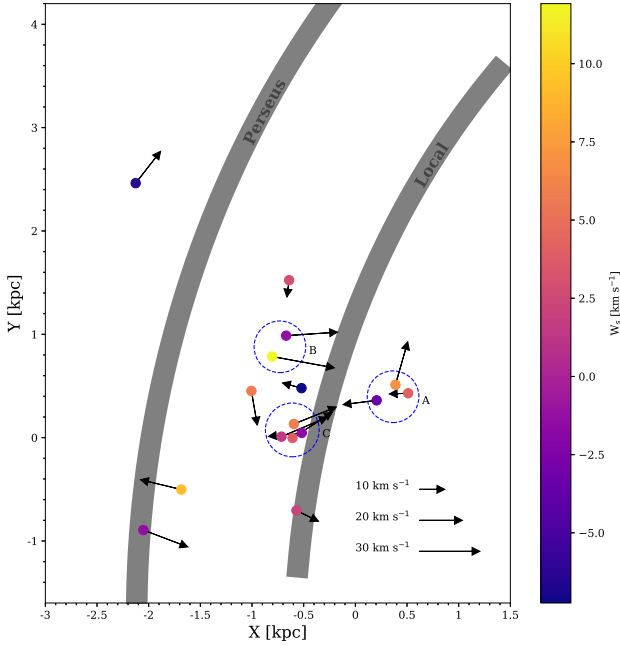
Fig. 7. Projection on the Galactic plane of the position and velocity with respect to the regional standard of rest of the clusters in our sample. The arrow sizes are proportional to v_{RSR} as shown. The points are coloured as a function of W_s. The shadow grey areas represent the spiral arms modelled by Reid et al. (2014).
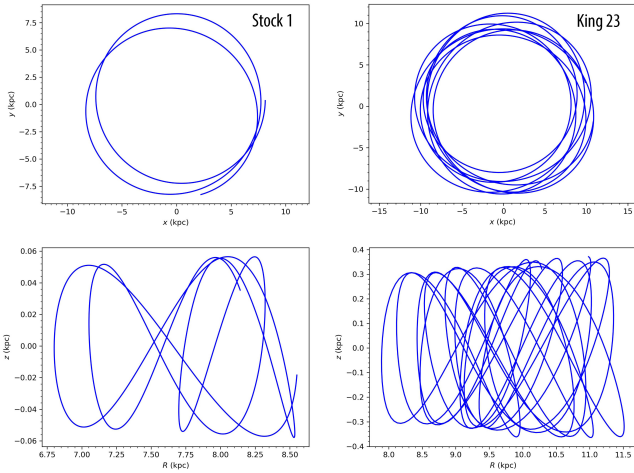

Fig. 8. Example of orbits for Stock 1 (*left*) and King 23 (*right*) with an age of 420 Ma and 1.95 Ga, respectively.

this may be explained by the fact that the orbits of the comparison sample by Tarricq et al. (2021) were computed only with *MW2014* potential without adding non-axisymmetric components. In fact, Tarricq et al. (2021) suggest that the OCs may be born in nearly circular orbits, but during their lives, the eccentricity of their orbits increases due to the perturbations with the non-axisymmetric Galaxy components, such as with spiral arms.

5.3. Open clusters' abundance ratios

As in the case of kinematics, it is interesting to check if the derived chemical abundances follow the trends described by the majority of open clusters. For this comparison, we used the large homogeneously analysed sample obtained by Spina et al. (2021) from the APOGEE and GALAH Galactic surveys.
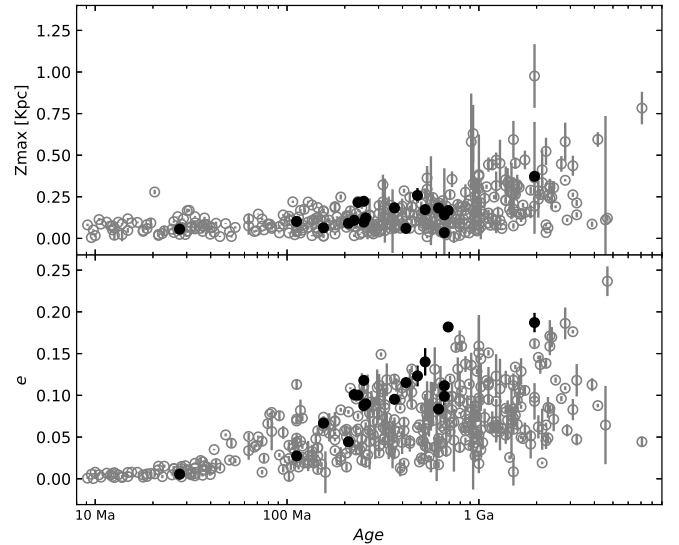

Fig. 9. Run of z_{max} (*top*) and eccentricity (*bottom*) as a function of age for the OCs from the high-quality sample (grey) of Tarricq et al. (2021) and for the OSTTA clusters studied here (black).

This sample contains 134 clusters for which abundances for 21 elements, from C to Eu, are provided. Unfortunately, this sample does not provide abundances for two of the elements studied, Sc and Ce. For this reason, we also used the abundances derived by Casamiquela et al. (2021) from spectra acquired with different instruments for stars around the red clump region belonging to 47 systems. Although this is a more limited sample with clusters in a radius of 500 pc with ages older than 200 Ma, it is still useful for our purpose. Finally, in the case of Ce, we added the comparison with the results obtained by Sales-Silva et al. (2022) from APOGEE infrared spectra.

The different [X/Fe] ratios as a function of [Fe/H] for our sample are shown in Fig. 10 and are colour-coded as a function of the age. The samples of Spina et al. (2021) and Casamiquela et al. (2021) are in light and dark grey, respectively.

The Na comparison is intriguing. There is no agreement between the two comparison samples. For the 14 clusters in common to both studies, the Spina et al. (2021) Na abundances are on average 0.24 dex higher than the Casamiquela et al. (2021) ones. Moreover, the Na abundances derived for the clusters studied here are higher than the Spina et al. (2021) ones. One explanation could be that our analysis did not take into account non-LTE corrections for the derived abundances, as is the case for Spina et al. (2021). However, in regards to Na, the abundances derived in LTE, as is also the case here, could be overestimated by up to 0.5 dex according to Lind et al. (2011). Moreover, as discussed by Casamiquela et al. (2020) (see also Smiljanic et al. 2016; Smiljanic & Gaia-ESO Survey Consortium 2018), the Na abundances could be affected by internal mixing in the surface of massive giants, which is related to the age of the clusters being more important for younger objects as observed in Fig. 10. The comparison for another light proton-capture element such as Al, which is less affected by non-LTE corrections in our case (e.g. Nordlander & Lind 2017), is in better agreement.

It is surprising that the three most metal-poor clusters studied, NGC 1027, NGC 1750, and Trumpler 2, are enhanced in Si by about 0.4 dex, but not in the other α-elements analysed (Mg, Ca, and Ti). The abundances for two of these clusters, NGC 1027 and NGC 1750, are based on only one star each, and therefore this result may be taken with caution. However, in the case of the
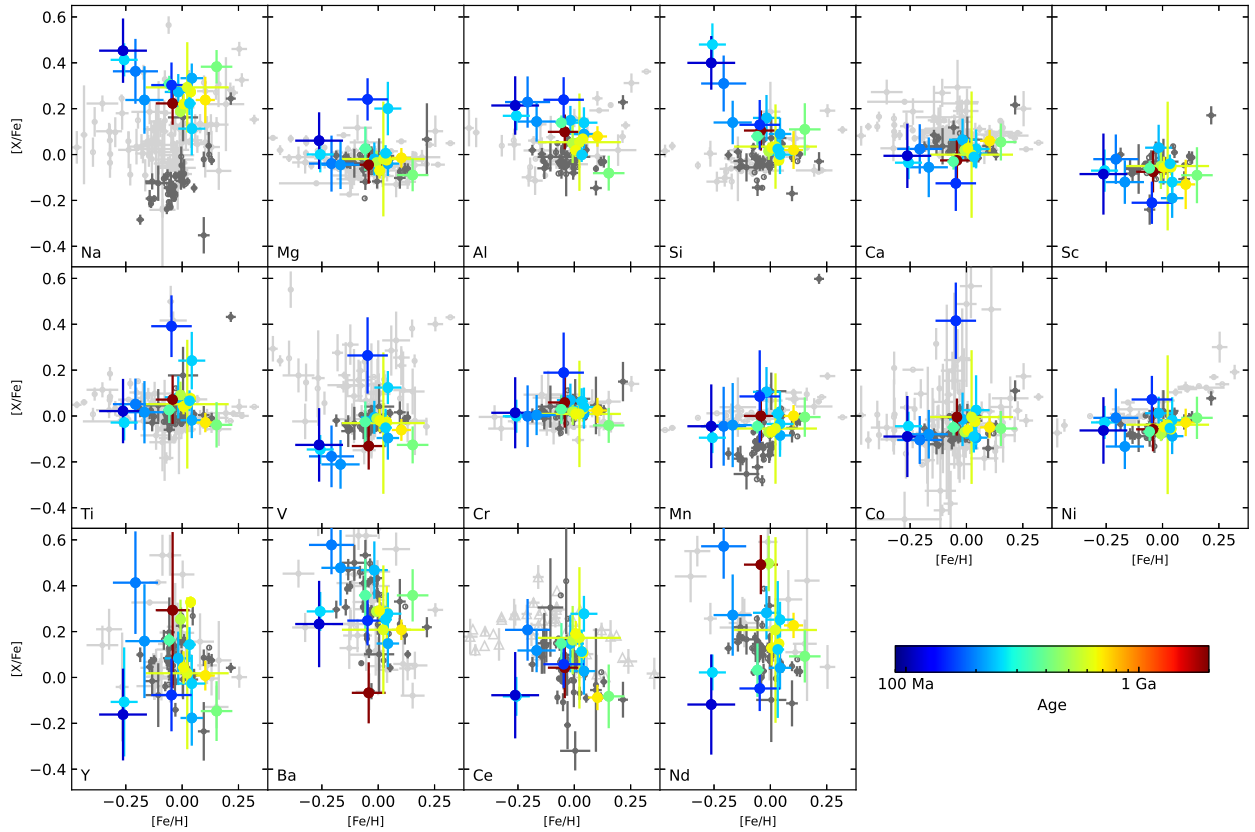
Fig. 10. Abundance ratios [X/Fe] versus [Fe/H] for the studied clusters, colour-coded as a function of their ages. Light and dark grey points are the OCs sampled by Spina et al. (2021) and Casamiquela et al. (2021), respectively. In the case of Ce, light grey triangles are the values obtained by Sales-Silva et al. (2022).

young, 110 Ma, Trumpler 2 system, we have analysed two stars and both have similar Si-enhanced abundances. The most probable explanation for this is the existing bias in Fe abundances as a function of $T_{\rm eff}$ and $\log g$, and thus with age, particularly affecting the youngest stars in our sample (Sect. 4.3). Since this bias tends to underestimate the Fe abundance of cooler stars, but not the Si abundance, we have probably obtained an underestimation of the [Fe/H] abundances and a net enhancement in [Si/Fe]. An enhancement in Si has been reported in another young (300 Ma, older than the three previously mentioned clusters) yet more metal-rich ([Fe/H] = 0.1 dex) cluster, NGC 6705 (Magrini et al. 2014; Casamiquela et al. 2018), but not by other works based on APOGEE data (e.g. Donor 2020; Spina et al. 2021). However, in this case, the Si enhancement is accompanied by an enhancement in Mg and O. The fact that no other [α/Fe] enhancement is obtained in these three clusters makes us think that they are most probably not α-enhanced objects.

Regardless, the existence of field stars with [Fe/H] in the range of the OCs and enhancements in α-element abundances have also been reported in the literature (e.g. Adibekyan et al. 2011; Martig et al. 2015; Chiappini et al. 2015). Three scenarios have been proposed for the origin of the young [α/Fe]-enhanced stars. The first assumes that the younger ages, which are determined from their masses, are wrong and that they are in fact older since their masses are higher than expected due to mass transfer from a binary companion, for instance, or they resulted from the merger of two stars (e.g. Martig et al. 2015; Izzard et al. 2018). This is not the case of OCs where ages are more accurately determined from their colour-magnitude diagrams. However, stars with a higher mass than expected have been found in at least two OCs where masses could be determined from

asteroseismology. Those high masses were explained as results of a merger or mass transfer in binary systems; for more information, readers can refer to Handberg et al. (2017) for NGC 6819 and Brogaard et al. (2021) for NGC 6791. The second scenario suggests that these objects are genuinely young, that they formed near the region of co-rotation of the Galactic bar, and that they have migrated to the solar neighbourhood (Chiappini et al. 2015). However, the orbits determined in previous sections suggest that the clusters were probably born roughly in the inner radius, but far enough away from the bar. An alternative is local self-enrichment due to the explosion of a supernova type II in a giant molecular cloud, as proposed by Magrini et al. (2015). According to these authors, a single explosion of a massive star with a mass in the range between 18 and 25 $M_\odot$ should be able to explain the Si abundances observed in these clusters. Moreover, the yields reported by Woosley & Weaver (1995) supported the higher enrichment in Si with respect to the other α-elements.

In the case of Ca, the abundances obtained here are slightly lower than those obtained by Spina et al. (2021), suggesting the existence of a zero-point between both samples. It is expected that [Ca/Fe] ~ 0.0 dex at solar metallicity (e.g. Magrini et al. 2014; Carrera et al. 2019). Therefore, the values reported by Spina et al. (2021) seem slightly overestimated.

A similar behaviour is observed in the case of V. For this element, it is interesting that the two metal-poor clusters in our sample have slightly lower abundances, although with large uncertainties. For the other refractory element, Sc, there is good agreement with the values reported by Casamiquela et al. (2021). Unfortunately, Spina et al. (2021) do not provide Sc abundances to compare with the values obtained here.

For the Fe-peak elements studied (Cr, Mn, Co, and Ni), there is agreement with the comparison samples within the uncertainties. The only noticeable feature is the enhancement of ~ 0.4 dex in Co for NGC 7654. This cluster also shows a similar enhancement in Ti. A single giant star was observed in this cluster, and therefore these results should be taken with caution. Moreover, there are doubts about the true membership of this star because the isochrones are not able to reproduce its positions in either the colour-magnitude (Fig. 1) or Kiel (Fig. 4) diagrams, as discussed before. The Spina et al. (2021) sample has other clusters with similar enhancements in Ti and Co. However, those systems with high Co abundances are not the same with a high Ti content.

Finally, the abundances derived for the four neutron capture elements analysed (Y, Ba, Ce, and Nd) are in agreement with the Spina et al. (2021) and Casamiquela et al. (2021) comparison samples taking into account the largest uncertainties in comparison to other elements involved in their determinations. In fact, the abundances of Ce and Nd are based on the measurements of a single weak line in each case: 527.4229 and 531.981 nm for Ce and Nd, respectively. The only noticeable feature is that two of the more metal-poor clusters (NGC 1750 and Trumpler 2) seem slightly out of the global trend. This result has to be taken with caution due to the large error bars, which prevent us from discussing this further. In the case of Ce, there is a clear shift between both our sample and the Casamiquela et al. (2021) samples with the values obtained by Sales-Silva et al. (2022) from APOGEE near-infrared spectra, which are slightly larger at any [Fe/H] value. Sales-Silva et al. (2022) quantified the difference with Casamiquela et al. (2021) in 0.16 dex. The differences may be due to the different solar reference abundances used in each case. Regardless, the trend reported by Sales-Silva et al. (2022) of increasing [Ce/Fe] with decreasing [Fe/H] until about [Fe/H] ~ 0.2 dex is also the case for the results obtained here.

5.4. Open clusters radial gradient

Another interesting feature of OCs is the run of [Fe/H] as a function of Galactocentric distance, $R_{\rm gc}$. It is widely accepted that [Fe/H] decreases as we move outwards, which seems to flatten when reaching a certain distance (e.g. Carrera & Pancino 2011; Magrini et al. 2017; Donor 2020). Unfortunately, the clusters studied here are located inside the breaking radius, and therefore they are not useful for investigating its location. However, it is interesting to compare the results obtained here with the majority of OCs.

In the top panel of Fig. 11, we plotted the run of [Fe/H] versus $R_{\rm gc}$ for the clusters studied here, which are colour-coded as a function of their age. As comparison samples, we have used the recent compilation obtained by Zhang et al. (2021), which includes 157 clusters from different sources, and the sample obtained by Spina et al. (2021) from the APOGEE and GALAH surveys described above. They are the dark and light grey points in Fig. 11. In general, the clusters studied here follow the trend described by the majority of open clusters. However, the existence of particular cases can be blurred when comparing all the clusters together, independently of their ages. In fact, it is known that the slope of the gradient changes with age, being steeper for the oldest clusters (e.g. Friel et al. 2002; Carrera & Pancino 2011; Donati et al. 2015; Donor 2020; Zhang et al. 2021). For this reason, in the rest of the panels of Fig. 11, we plotted three different age ranges. The clusters studied here follow, within the uncertainties, the trends described by coeval systems without noticeable differences.
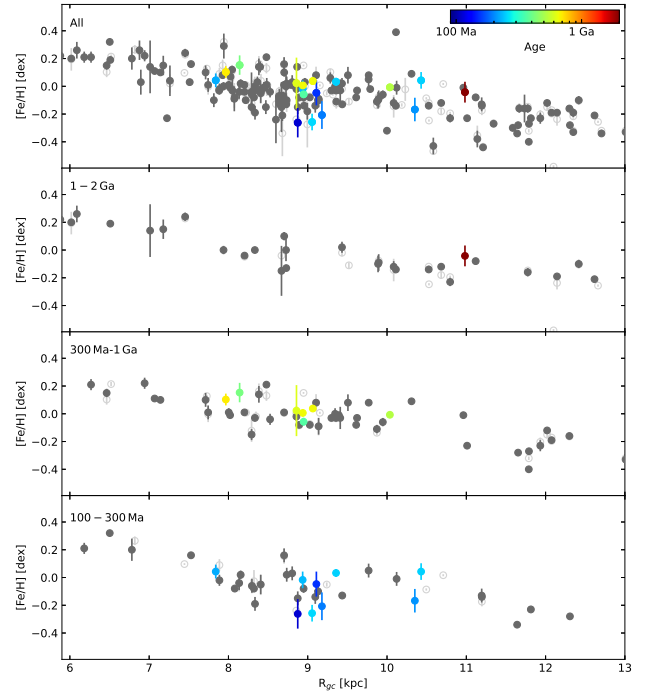

Fig. 11. Run of [Fe/H] versus $R_{\rm gc}$ for the studied clusters, colour-coded as a function of their age. Dark and light grey points are the clusters in Zhang et al. (2021) and Spina et al. (2021), respectively, which are plotted for comparison. *Top panel*: whole sample, while the remaining panels show three different age ranges.

6. Conclusions

The OSTTA project was designed to provide high resolution follow-up spectroscopy of poorly studied open clusters. In this paper, we derived radial velocities for 41 stars belonging to 20 open clusters, including the following four systems recently discovered from *Gaia* data releases: COIN-*Gaia* 2, COIN-*Gaia* 6, Gulliver 37, and UBC 54.

To our knowledge, our analysis provides the first radial velocity determination based on high resolution spectroscopy for most of the studied clusters. At the time of writing, only *Gaia* radial velocities were available for most of them. The radial velocities allowed us to detect four potential spectroscopic binaries and to revise the membership of each cluster, discarding four objects. After this procedure, we cannot be sure that we sampled a true member of Gulliver 37 since the star observed in this cluster was reported as a variable in the literature.

Atmospheric parameters were determined for the 32 stars considered as cluster members from their radial velocities. Two stars have very low gravities, which is an indication of being supergiant stars. For two objects, we were not able to properly constrain the atmospheric parameters due to the low S/N of their spectra. Likewise, we were not able to constrain the atmospheric parameters of the star observed in NGC 581, which was reported in the literature as an M supergiant. Abundances for 17 chemical species were determined in the remaining 28 stars belonging to 17 open clusters. To our knowledge, this is the first chemical abundance determination for most of them.

We investigated the behaviour of the studied clusters in the framework of the majority of the open clusters. All the studied clusters show typical thin disc kinematics, and their orbits are also within the ranges described by the majority of open clusters.

The derived abundance ratios follow the general trends described by the majority of clusters. However, we found that three young clusters, NGC 1027, NGC 1750, and Trumpler 2, are enhanced in Si without signs of enrichment in the other α-elements studied (Mg, Ca, and Ti). This behaviour was only observed previously in another young cluster, NGC 6705. There is no clear explanation for the abundances measured in these clusters. Finally, we confirmed that the [Fe/H] abundances derived for the studied clusters follow the radial gradient traced by other clusters of similar ages.

References

Adibekyan, V. Z., Santos, N. C., Sousa, S. G., & Israelian, G. 2011, A&A, 535, L11
Akbulut, B., Ak, S., Yontan, T., et al. 2021, Ap&SS, 366, 68
Allende Prieto, C., Beers, T. C., Wilhelm, R., et al. 2006, ApJ, 636, 804
Allende Prieto, C., Koesterke, L., Hubeny, I., et al. 2018, A&A, 618, A25
Alonso-Santiago, J., Negueruela, I., Marco, A., et al. 2019, A&A, 631, A124
Antoja, T., Figueras, F., Romero-Gómez, M., et al. 2011, MNRAS, 418, 1423
Astropy Collaboration (Robitaille, T. P., et al.). 2013, A&A, 558, A33
Astropy Collaboration (Price-Whelan, A. M., et al.). 2018, AJ, 156, 123
Baratella, M., D'Orazi, V., Carraro, G., et al. 2020, A&A, 634, A34
Baratella, M., D'Orazi, V., Sheminova, V., et al. 2021, A&A, 653, A67
Bertelli Motta, C., Pasquali, A., Richer, J., et al. 2018, MNRAS, 478, 425
Binney, J., & Tremaine, S. 2008, Galactic Dynamics, 2nd edn. (Princeton: Princeton University Press)
Blanco-Cuaresma, S. 2019, MNRAS, 486, 2075
Blanco-Cuaresma, S., Soubiran, C., Heiter, U., & Jofré, P. 2014, A&A, 569, A111
Bossini, D., Vallenari, A., Bragaglia, A., et al. 2019, A&A, 623, A108
Bovy, J. 2015, ApJS, 216, 29
Bovy, J., Leung, H. W., Hunt, J. A. S., et al. 2019, MNRAS, 490, 4740
Bragaglia, A., & Tosi, M. 2006, AJ, 131, 1544
Bragaglia, A., Alfaro, E. J., Flaccomio, E., et al. 2022, A&A, 659, A200
Brogaard, K., Arentoft, T., Jessen-Hansen, J., & Miglio, A. 2021, MNRAS, 507, 496
Cantat-Gaudin, T., Jordi, C., Vallenari, A., et al. 2019, A&A, 618, A93
Cantat-Gaudin, T., Anders, F., Castro-Ginard, A., et al. 2020, A&A, 640, A1
Carrera, R., & Pancino, E. 2011, A&A, 535, A30
Carrera, R., Bragaglia, A., Cantat-Gaudin, T., et al. 2019, A&A, 623, A80
Carrera, R., Casamiquela, L., Carbajo-Hijarrubia, J., et al. 2022, A&A, 658, A14
Casamiquela, L., Carrera, R., Jordi, C., et al. 2016, MNRAS, 458, 3150
Casamiquela, L., Carrera, R., Blanco-Cuaresma, S., et al. 2017, MNRAS, 470, 4363
Casamiquela, L., Carrera, R., Balaguer-Núñez, L., et al. 2018, A&A, 610, A66
Casamiquela, L., Tarricq, Y., Soubiran, C., et al. 2020, A&A, 635, A8
Casamiquela, L., Soubiran, C., Jofré, P., et al. 2021, A&A, 652, A25
Castro-Ginard, A., Jordi, C., Luri, X., et al. 2018, A&A, 618, A59
Castro-Ginard, A., Jordi, C., Luri, X., Cantat-Gaudin, T., & Balaguer-Núñez, L. 2019, A&A, 627, A35
Castro-Ginard, A., Jordi, C., Luri, X., et al. 2020, A&A, 635, A45

Chiappini, C., Anders, F., Rodrigues, T. S., et al. 2015, A&A, 576, L12
Cox, D. P., & Gómez, G. C. 2002, ApJS, 142, 261
Cropper, M., Katz, D., Sartoretti, P., et al. 2018, A&A, 616, A5
Dalton, G., Trager, S. C., Abrams, D. C., et al. 2012, SPIE Conf. Ser., 8446, 84460P
De Silva, G. M., Freeman, K. C., Bland-Hawthorn, J., et al. 2015, MNRAS, 449, 2604
Dias, W. S., Monteiro, H., Moitinho, A., et al. 2021, MNRAS, 504, 356
Donati, P., Cocozza, G., Bragaglia, A., et al. 2015, MNRAS, 446, 1411
Donor, J., Frinchaboy, P. M., Cunha, K., et al. 2020, AJ, 159, 199
Ferrers, N. 1877, Q. J. Pure Appl. Math., 14, 1
Freeman, K., & Bland-Hawthorn, J. 2002, ARA&A, 40, 487
Friel, E. D., Janes, K. A., Tavarez, M., et al. 2002, AJ, 124, 2693
Gaia Collaboration (Prusti, T., et al.). 2016, A&A, 595, A1
Gaia Collaboration (Brown, A. G. A., et al.). 2021, A&A, 649, A1
Gilmore, G., Randich, S., Asplund, M., et al. 2012, The Messenger, 147, 25
Gray, R. O., & Corbally, C. J. 1994, AJ, 107, 742
Guiglion, G., Battistini, C., Bell, C. P. M., et al. 2019, The Messenger, 175, 17
Gustafsson, B., Edvardsson, B., Eriksson, K., et al. 2008, A&A, 486, 951
Handberg, R., Brogaard, K., Miglio, A., et al. 2017, MNRAS, 472, 979
Heiter, U., Lind, K., Bergemann, M., et al. 2021, A&A, 645, A106
Holanda, N., Pereira, C. B., & Drake, N. A. 2019, MNRAS, 482, 5275
Hunter, J. D. 2007, Comput. Sci. Eng., 9, 90
Izzard, R. G., Preece, H., Jofre, P., et al. 2018, MNRAS, 473, 2984
Jeffries, R. D., Jackson, R. J., Cottaar, M., et al. 2014, A&A, 563, A94
Jenkins, A., & Binney, J. 1990, MNRAS, 245, 305
Katz, D., Sartoretti, P., Cropper, M., et al. 2019, A&A, 622, A205
Keenan, P. C., & McNeil, R. C. 1989, ApJS, 71, 245
Kovtyukh, V. V. 2007, MNRAS, 378, 617
Lagarde, N., Decressin, T., Charbonnel, C., et al. 2012, A&A, 543, A108
Lind, K., Asplund, M., Barklem, P. S., & Belyaev, A. K. 2011, A&A, 528, A103
Luck, R. E. 2014, AJ, 147, 137
Magrini, L., Randich, S., Romano, D., et al. 2014, A&A, 563, A44
Magrini, L., Randich, S., Donati, P., et al. 2015, A&A, 580, A85
Magrini, L., Randich, S., Kordopatis, G., et al. 2017, A&A, 603, A2
Majewski, S. R., Schiavon, R. P., Frinchaboy, P. M., et al. 2017, AJ, 154, 94
Mapelli, M., Vallenari, A., Jeffries, R. D., et al. 2015, A&A, 578, A35
Marigo, P., Girardi, L., Bressan, A., et al. 2017, ApJ, 835, 77
Martig, M., Rix, H.-W., Silva Aguirre, V., et al. 2015, MNRAS, 451, 2230
Mermilliod, J. C., Mayor, M., & Udry, S. 2008, A&A, 485, 303
Navarro, J. F., Frenk, C. S., & White, S. D. M. 1997, ApJ, 490, 493
Netopil, M., Paunzen, E., Heiter, U., & Soubiran, C. 2016, A&A, 585, A150
Netopil, M., Oralhan, İ. A., Çakmak, H., Michel, R., & Karataş, Y. 2022, MNRAS, 509, 421
Nordlander, T., & Lind, K. 2017, A&A, 607, A75
Pedregosa, F., Varoquaux, G., Gramfort, A., et al. 2011, J. Mach. Learn. Res., 12, 2825
Randich, S., Gilmore, G., & Gaia-ESO Consortium. 2013, The Messenger, 154, 47
Reddy, A. B. S., Lambert, D. L., & Giridhar, S. 2016, MNRAS, 463, 4366
Reid, M. J., Menten, K. M., Brunthaler, A., et al. 2014, ApJ, 783, 130
Riello, M., De Angeli, F., Evans, D. W., et al. 2021, A&A, 649, A3
Roederer, I. U., Preston, G. W., Thompson, I. B., et al. 2014, AJ, 147, 136
Romero-Gómez, M., Athanassoula, E., Antoja, T., & Figueras, F. 2011, MNRAS, 418, 1176
Romero-Gómez, M., Figueras, F., Antoja, T., Abedi, H., & Aguilar, L. 2015, MNRAS, 447, 218
Sales-Silva, J. V., Daflon, S., Cunha, K., et al. 2022, ApJ, 926, 154
Schönrich, R., Binney, J., & Dehnen, W. 2010, MNRAS, 403, 1829
Smiljanic, R., & Gaia-ESO Survey Consortium. 2018, IAU Symp., 334, 128
Smiljanic, R., Romano, D., Bragaglia, A., et al. 2016, A&A, 589, A115
Smiljanic, R., Donati, P., Bragaglia, A., Lemasle, B., & Romano, D. 2018, A&A, 616, A112
Soubiran, C., Cantat-Gaudin, T., Romero-Gómez, M., et al. 2018, A&A, 619, A155
Spina, L., Ting, Y. S., De Silva, G. M., et al. 2021, MNRAS, 503, 3279
Spitzer, Lyman, J., & Schwarzschild, M. 1951, ApJ, 114, 385
Tarricq, Y., Soubiran, C., Casamiquela, L., et al. 2021, A&A, 647, A19
Taylor, M. B. 2005, ASP Conf. Ser., 347, 29
Telting, J. H., Avila, G., Buchhave, L., et al. 2014, Astron. Nachr., 335, 41
Tonry, J., & Davis, M. 1979, AJ, 84, 1511
Trumpler, R. J., & Weaver, H. F. 1953, Statistical Astronomy, 256
Valenti, J. A., & Fischer, D. A. 2005, ApJS, 159, 141
Wenger, M., Ochsenbein, F., Egret, D., et al. 2000, A&AS, 143, 9
Woosley, S. E., & Weaver, T. A. 1995, ApJS, 101, 181
Zhang, R., Lucatello, S., Bragaglia, A., et al. 2021, A&A, 654, A77

Appendix A: Notes on individual clusters

All the *Gaia* identifications used in this section refer to *Gaia* EDR3, except where otherwise specified.

ASCC 23   The radial velocity of the star observed in this cluster, with $p=1$, is in good agreement within the uncertainties with the values reported by Soubiran et al. (2018) and Tarricq et al. (2021) derived from six and nine stars, respectively. Therefore, we consider it as representative of the radial velocity of the cluster.

Alessi 44   A single exposure has been acquired for the star observed in Alessi 44. The derived radial velocity is in agreement with the values available in the literature by Soubiran et al. (2018) and Tarricq et al. (2021) derived from seven and nine stars, respectively. Therefore, although this star has $p=0.5$, we consider it as representative of the cluster.

Alessi 62   Two out of three stars observed in Alessi 62 have $p=1$ and compatible radial velocities. The third star, 45193335743607072, was observed; although, it has a negligible membership probability. Its derived radial velocity is very different from the other two and from the value provided by *Gaia* DR2 for it. Coupled with the large radial velocity uncertainty of $\sim5\,\mathrm{km\,s^{-1}}$ reported by *Gaia* , this suggests that this object might be a spectroscopic binary. The average velocity derived from two member stars is in good agreement with the values found by Soubiran et al. (2018) and Tarricq et al. (2021) from 12 and ten stars, respectively.

COIN-Gaia 2   Two of the observed stars in this cluster have $p=1$. The other one, 423486180567313024, has a very low value, $p=0.05$. In fact, its radial velocity differs by $\sim3\,\mathrm{km\,s^{-1}}$ from that of the other two. We consider this star as a non-member, but it could also be a spectroscopic binary.

COIN-Gaia 6   The three observed stars have very high astrometric membership probabilities and similar radial velocities among them. However, the average radial velocity derived for this cluster significantly differs from the value reported by Tarricq et al. (2021): $-47.26\pm2.41\,\mathrm{km\,s^{-1}}$, derived from *Gaia* DR2 measures of three stars. There are two stars in common between both samples, 506224812820610176 and 506223988186933888. Whereas there is good agreement between the radial velocities derived here and those provided by Tarricq et al. (2021) for one star, there is a difference of $\sim3\,\mathrm{km\,s^{-1}}$ for the other. The *Gaia* DR2 radial velocity uncertainty for this object is $2.69\,\mathrm{km\,s^{-1}}$. This, together with the small discrepancy between both studies, could be a hint that this star is a spectroscopic binary. The additional star used by Tarricq et al. (2021), which is not in common with our sample, has a significantly lower radial velocity $-51.3\pm0.2\,\mathrm{km\,s^{-1}}$ in *Gaia* DR2 and a lower astrometric membership probability, 0.47. This slightly discrepant star as well as the previously mentioned discrepant object in common are the cause of the difference in the average v_{rad}. In our study, however, the three radial velocities are in very good agreement and with consistent low uncertainties, thus we consider the three stars to be real cluster members.

FSR 0951   The three stars observed have $0.5\leq p\leq0.9$. The star 3368695854168200192, with the lower astrometric membership probability, $p=0.5$, has a slightly different v_{rad}. The *Gaia* DR2 radial velocity for this star, $46.15\pm0.38\,\mathrm{km\,s^{-1}}$, is in good agreement with our measurement. Comparing this with *Gaia* EDR3 mean proper motions and parallaxes, this star has μ_α outside three sigma from the mean cluster value listed in Table 1. We discarded this object in our analysis. From the remaining stars, we obtained an average radial velocity of $43.80\pm0.48\,\mathrm{km\,s^{-1}}$, which is compatible with the value reported by Soubiran et al. (2018) and Tarricq et al. (2021) from five stars in both cases.

Gulliver 37   The only star sampled in this cluster, 2024469226291472000, has $p=0.9$. The radial velocity obtained here, $21.92\pm0.02\,\mathrm{km\,s^{-1}}$, is quite different from the value provided by *Gaia* DR2 of $2.5\pm8.2\,\mathrm{km\,s^{-1}}$ for the same star. Recently, this star was observed in the framework of the Stellar Population Astrophysics (SPA) project by Zhang et al. (2021) who obtained a radial velocity of $-4.59\pm0.17\,\mathrm{km\,s^{-1}}$. Due to the large velocity dispersion reported by *Gaia* DR2 and the discrepancy among the different radial velocity determinations available, we consider this object as a potential spectroscopic binary, although our spectrum did not show either significant wide lines or double lines. Therefore, we cannot ensure that it is a real cluster member, and we excluded this cluster from our analysis.

King 23   The three stars observed in King 23 have $p\geq0.8$. The derived radial velocity for one of them, 3109989396744298624, differs by $\sim3\,\mathrm{km\,s^{-1}}$ from the other two. A similar difference between the radial velocities of the discrepant star and the other two is observed in the values provided by *Gaia* DR2. Since there is no hint of it being a spectroscopic binary, we discarded it from our analysis. The average radial velocity provided by Soubiran et al. (2018) and Tarricq et al. (2021) for this cluster, obtained from the *Gaia* DR2 velocities of four stars, slightly differs from the value found here because of the contamination of the discrepant star.

NGC 581   The single star observed has $p=0.8$. This star was catalogued as an M supergiant (M0.5Ib-II) by Keenan & McNeil (1989) and reported as variable by Mermilliod et al. (2008). The derived radial velocity is compatible with the *Gaia* DR2 value. Neither our measure nor the *Gaia* DR2 one shows a sign of radial velocity variability. The average values for this cluster provided by Soubiran et al. (2018), for this same star, and by Tarricq et al. (2021), for two stars, are in agreement with the value found here. We assumed that this star is a real cluster member, although this should be confirmed in the future by sampling other stars. However, we discarded this object in the chemical analysis because it is an M supergiant.

NGC 1027   The two stars observed in this cluster have $p=1$, 465682692367536384, and 0.8, 465853425905007872, respectively. However, we found very different radial velocities for each of them. *Gaia* DR2 also provides radial velocities for these stars which are in good agreement with our individual measurements within the uncertainties. There is a significant difference between the values provided for this cluster by Soubiran et al. (2018) from one star $-4.06\pm0.31\,\mathrm{km\,s^{-1}}$, and Tarricq et al. (2021) from six stars $-36.57\pm10.83\,\mathrm{km\,s^{-1}}$. The value found by Tarricq

et al. (2021) is in agreement with the radial velocity derived for the star 465682692367536384 within the uncertainties. For this reason, we consider this star as a real member of the cluster, although this assumption should be confirmed in the future.

NGC 1647   The two stars observed in this cluster have p=1 and compatible radial velocities within the uncertainties. The derived radial velocities are in agreement with the values reported by *Gaia* DR2 and Mermilliod et al. (2008) within the uncertainties. The obtained average radial velocity is in good agreement with the values provided by Soubiran et al. (2018) and Tarricq et al. (2021) from 16 and 21 stars, respectively.

NGC 1750   The two observed stars have p=1 (3418663507987229184) and p=0.8 (3418709412597592576). However, their radial velocities differ by ~3 km s^{-1}. *Gaia* DR2 provided radial velocities for these two objects. There is good agreement for star 3418663507987229184. However, for 3418709412597592576, there is a difference of about 2 km s^{-1}; although, the *Gaia* DR2 value has an uncertainty of 1.1 km s^{-1}, which could be a sign that this star is a spectroscopic binary. The value that we found for the first star is also in agreement with the average radial velocity provided by Soubiran et al. (2018) for this cluster, -10.38±2.31 km s^{-1} , from seven stars, including the two observed here. Tarricq et al. (2021) provide a significantly different value, -7.45 km s^{-1}, but with a larger uncertainty, 6.64 km s^{-1}, from 13 stars. The star 3418709412597592576 is slightly displaced from the isochrone, but we see that the isochrone is not a perfect match for the cluster sequence, mainly at the main sequence turn-off (see Fig. 1). Therefore, with all the information in hand, we assume that star 3418663507987229184 is representative of the cluster, although this assumption should be confirmed in following studies.

NGC 2186   The single observed star has p=1. The obtained radial velocity is compatible within uncertainties with the value determined by Mermilliod et al. (2008) and with that provided by *Gaia* DR2. Moreover, this is the only star used by Soubiran et al. (2018) as a representative of this cluster. The value used by Tarricq et al. (2021) for this star is 20.98±0.78 km s^{-1}, which is also compatible with our value. These authors determined an average radial velocity for this cluster of 21.71±4.01 km s^{-1} obtained from three stars. All together, we consider the observed star as a real cluster member.

NGC 2281   The two stars observed in this system have p=1 and similar radial velocities within the uncertainties. Moreover, the obtained velocities are in agreement with *Gaia* DR2, Mermilliod et al. (2008), and Luck (2014), again, within the uncertainties. The obtained average radial velocity is in agreement with the values provided by Soubiran et al. (2018) and Tarricq et al. (2021) from 42 and 40 stars, respectively, and also from the values obtained by Smiljanic et al. (2018) for two objects in this cluster.

NGC 2345   We have observed three objects in NGC 2345 with p ≥0.9. One of them, 3044669506889464320, was reported as a spectroscopic binary by Mermilliod et al. (2008). The derived radial velocity for this star significantly differs from the values for the other two. A similar difference is observed in the *Gaia* DR2 radial velocities, which are in agreement with the values

obtained here. The average radial velocity obtained by discarding this object, 58.41±0.15 km s^{-1}, slightly differs from the values reported by Soubiran et al. (2018), 60.94 km s^{-1}, and Tarricq et al. (2021), 63.27 km s^{-1}, from six stars in both cases, but they reported large dispersions of 4.89 and 2.43 km s^{-1}, respectively. It is worth mentioning that Alonso-Santiago et al. (2019) report an average radial velocity for this cluster of 58.5±0.5 km s^{-1} from four stars, including the two used here.

NGC 2358   The three stars observed have 0.6≤ p ≤0.9. The radial velocities of the three objects are similar within the uncertainties, and also they are compatible with the average values derived from *Gaia* DR2 velocities. In fact, the average radial velocity obtained, 28.31±0.85 km s^{-1}, is compatible within the uncertainties with the values provided by Soubiran et al. (2018), 27.57±1.03 km s^{-1}, and Tarricq et al. (2021), 27.57±0.6 km s^{-1}, from the same three stars.

NGC 7654   The two stars observed in this cluster have p=1 and similar radial velocities within the uncertainties between them and with the values provided by *Gaia* DR2. The average radial velocity is in agreement with the values provided by Soubiran et al. (2018) and Tarricq et al. (2021) because they were obtained from the *Gaia* DR2 velocities for the same stars. Both stars are far away from the expected location for the red clump for the age of this cluster (Fig. 1), suggesting a younger age. Recently, Akbulut et al. (2021) revised the age of this cluster to a slightly younger value of 120 Ma, which is still insufficient to reproduce the position of these stars in the colour-magnitude diagram. The same authors highlight that in order to reproduce the position of these stars, an isochrone of about 40 Ma would be needed. In this case, the observed stars would be supergiants. Owing to the agreement in the radial velocities of the two observed stars, and also in the derived chemical abundances (see next section), we consider them as real clusters members. However, this is an assumption that should be taken with caution until their membership is confirmed with the radial velocities of other objects in the main sequence.

Stock 1   We have acquired a single exposure for one star in this cluster, which has p=1. The derived radial velocity is in good agreement with the values determined from *Gaia* DR2 by Soubiran et al. (2018) and Tarricq et al. (2021) from 30 and 29 objects, respectively. Therefore, we consider the star as a real cluster member and the derived radial velocity as representative of the cluster.

Trumpler 2   The two stars observed in this system have p=0.9 and similar radial velocities within their uncertainties and also with the values provided by *Gaia* DR2. The derived average radial velocity is in good agreement with the values obtained by Soubiran et al. (2018) and Tarricq et al. (2021) from 11 and 12 objects, respectively. One star in this cluster was sampled by Smiljanic et al. (2018) who found a compatible radial velocity with the value obtained here.

UBC 54   The two stars observed in this cluster have p=1. The obtained radial velocities are in agreement within the uncertainties and also with *Gaia* DR2. The average radial velocity is compatible within the uncertainties with the value provided by Tarricq et al. (2021) from the same two stars measured by *Gaia* DR2.

Appendix B: Some extra material

Table B.1. Observing log and radial velocities

Cluster	Gaia ID EDR3	RA deg	DEC deg	G-band mag	S/N pix^{-1}	N	texp s	Date	v_{rad} km s^{-1}	v_{scatter} km s^{-1}	v_{err} km s^{-1}	Notes
ASCC 23	9685120002808979456	95.039717	46.646874	7.747	91.4	3	120	14/12/2018	-13.347	0.019	0.025	
Alessi 44	4239077200124649216	294.322473	-0.492237	7.873	98.1	1	180	24/04/2019	-9.578		1.108	
Alessi 62	4519333643079413760	284.069306	21.548663	9.926	137.9	3	1800	18/04/2019	12.873	0.009	0.013	
Alessi 62	4519335601584434048	284.050962	21.65614	9.687	143.6	3	1800	18/04/2019	13.054	0.014	0.049	
Alessi 62	4519300898247954560	283.905531	21.265434	9.911	155.5	3	1800	19/04/2019	21.1	0.009	0.025	SB?/NM
COIN Gaia2	423486184877336448	15.076727	55.375846	10.181	87.8	3	1900	12/12/2018	-35.512	0.018	0.048	NM
COIN Gaia2	423487731065542272	14.998977	55.45639	10.69	108.8	3	2100	12/12/2018	-32.721	0.02	0.039	
COIN Gaia2	423486184872160128	15.086556	55.367102	10.736	102.8	3	2100	12/12/2018	-32.39	0.023	0.018	
COIN Gaia6	5062223988186933888	28.052953	58.561446	10.377	85.6	3	1500	14/12/2018	-42.319	0.002	0.009	
COIN Gaia6	5062224812820610176	28.049522	58.642991	13.144	52.7	3	10800	14/12/2018	-42.118	0.029	0.109	SB?/low S/N
COIN Gaia6	5062214401820077056	28.156907	58.629604	13.331	48.1	3	10800	15/12/2018	-42.811	0.004	0.158	low S/N
FSR 0951	3344673277448107776	95.603076	14.476332	11.526	132.7	6	9000	12,16/12/2018	43.462	0.042	0.025	
FSR 0951	3344692140944457088	95.351933	14.667711	11.574	133.8	6	9000	12,15/12/2018	44.137	0.042	0.034	
FSR 0951	3368695854168200192	95.689046	14.61152	11.352	136.7	6	8400	13,14/12/2018	46.279	0.027	0.032	NM
Gulliver 37	2024469226291472000	292.076836	25.381498	10.592	101.7	3	2700	19/04/2019	21.92	0.024	0.051	SB
King 23	3109989396744298624	110.428062	-0.963394	12.123	91.9	3	8100	13/12/2018	56.471	0.008	0.004	NM
King 23	3109989392447848960	110.440528	-0.960479	12.263	97.7	3	8100	13/12/2018	53.67	0.008	0.006	
King 23	3109989121872110080	110.46442	-0.981852	12.373	83.8	3	8100	14/12/2018	53.846	0.019	0.005	
NGC 581	509862169090128000	23.371715	60.646584	7.437	84.9	4	260	14/12/2018	-46.782	0.008	0.021	Variable/M supergiant
NGC 1027	465682692367536384	40.577551	61.737139	8.077	82.4	3	360	16/12/2018	-43.317	0.017	0.012	
NGC 1027	465853425905007872	39.571876	61.578574	10.138	84.8	3	2600	16/12/2018	-2.322	0.013	0.013	NM
NGC 1647	3409869064229856128	71.521245	18.800733	6.91	197.0	3	360	16/12/2018	-6.351	0.008	0.01	
NGC 1647	3410117313342257664	71.649563	19.494243	7.784	118.8	3	360	16/12/2018	-6.483	0.013	0.042	
NGC 1750	3418663507987229184	76.087212	23.527111	6.892	191.0	3	360	14/12/2018	-10.065	0.009	0.008	
NGC 1750	3418709412597592576	76.200009	23.920917	7.205	182.4	3	360	14/12/2018	-13.481	0.014	0.018	SB?/NM
NGC 2186	3318650315417696384	93.026044	5.464272	9.486	137.4	3	2400	16/12/2018	20.821	0.017	0.071	
NGC 2281	951479674341906560	102.062876	41.072802	8.69	80.3	3	160	14/12/2018	19.552	0.016	0.018	
NGC 2281	951676899239237632	102.090499	41.302284	6.857	158.8	3	120	14/12/2018	19.407	0.009	0.005	
NGC 2345	3044669232011557760	107.109659	-13.187338	9.891	71.8	3	1100	15/12/2018	58.598	0.027	0.017	
NGC 2345	3044669506889464320	107.091051	-13.173124	9.234	78.2	3	1400	15/12/2018	64.078	0.027	0.118	SB
NGC 2345	3044665967836430976	107.126537	-13.231258	9.706	91.1	3	2300	15/12/2018	58.384	0.01	0.032	
NGC 2358	2934838637556373888	109.256039	-17.151366	9.634	132.4	3	2400	15/12/2018	28.496	0.006	0.005	
NGC 2358	2934861658580860928	109.314538	-16.888067	9.117	226.8	3	2400	15/12/2018	27.003	0.015	0.008	
NGC 2358	2934834411310429824	109.317203	-17.221546	9.992	160.2	3	2400	15/12/2018	28.56	0.019	0.048	
NGC 7654	2015645057006454144	351.186937	61.344091	8.202	81.9	6	910	15/12/2018	-32.012	0.014	0.021	
NGC 7654	2015663649928489856	351.066006	61.588202	7.855	126.6	3	900	15/12/2018	-32.199	0.009	0.057	
Sotck 1	2021217798603195264	294.47485	24.712883	7.774	102.2	1	180	19/04/2019	19.605		0.238	
Trumpler 2	457691785453711360	39.169356	56.196734	6.814	194.2	3	360	15/12/2018	-3.781	0.001	0.012	
Trumpler 2	454676374812927744	39.220012	55.915377	6.783	191.5	3	360	15/12/2018	-3.881	0.012	0.007	
UBC 54	2330049705784504576	64.672277	46.209049	9.799	114.5	3	2400	15/12/2018	-15.278	0.017	0.02	
UBC 54	2338207726744047360	64.714494	46.561861	9.921	110.2	3	2400	16/12/2018	-15.138	0.005	0.025	

Notes. (NM) nom-member; (SB) spectroscopic binary.

Table B.2. Effective temperatures, surface gravities, and global metallicities obtained from the spectroscopic analysis of the observed stars. The CDS version includes all the individual abundances.

cluster	star	T_{eff} [K]	$\log g$	[M/H]	[Fe/H]
ASCC 23	968512002808979456	5022 ± 18	2.24 ± 0.05	−0.05	−0.02 ± 0.06
Alessi 44	4240034050119188352	4667 ± 10	1.69 ± 0.05	−0.08	0.04 ± 0.05
Alessi 62	4519333643079413760	5027 ± 13	2.76 ± 0.03	−0.02	0.07 ± 0.05
Alessi 62	4519335601584434048	5032 ± 14	2.65 ± 0.03	0.03	0.13 ± 0.05
COIN-Gaia 2	423486184872160128	5133 ± 16	2.72 ± 0.03	0.00	0.05 ± 0.05
COIN-Gaia 2	423487726755535232	5144 ± 21	2.71 ± 0.06	−0.03	0.02 ± 0.05
COIN-Gaia 6	5062239881869333888	3929 ± 12	0.27 ± 0.05	−0.50	
COIN-Gaia 6	5062144018200770056	5702 ± 30	2.61 ± 0.07	0.76	
COIN-Gaia 6	5062248128206101756	5489 ± 31	2.18 ± 0.07	0.58	
FSR 0951	3344692140944457088	5152 ± 13	2.63 ± 0.04	−0.06	0.00 ± 0.06
FSR 0951	3344673277448107776	5180 ± 14	2.60 ± 0.03	−0.07	−0.02 ± 0.05
King 23	3109989392447848960	4492 ± 15	2.07 ± 0.03	−0.10	−0.07 ± 0.07
King 23	3109989121872110080	4619 ± 15	2.21 ± 0.03	−0.07	−0.02 ± 0.08
NGC 1027	465682692367536384	4160 ± 14	1.07 ± 0.03	−0.23	−0.21 ± 0.10
NGC 1647	3410117313341005184	4696 ± 11	1.81 ± 0.05	−0.16	−0.08 ± 0.07
NGC 1647	3409869064229856128	4914 ± 9	1.80 ± 0.02	−0.13	−0.04 ± 0.05
NGC 1750	3418663507987229184	4128 ± 8	1.10 ± 0.02	−0.32	−0.26 ± 0.06
NGC 2186	3318650315417696384	5686 ± 14	1.72 ± 0.04	−0.05	0.04 ± 0.06
NGC 2281	951676899239237632	4451 ± 8	1.74 ± 0.03	−0.18	−0.11 ± 0.04
NGC 2281	951479674341906560	5199 ± 12	2.81 ± 0.04	0.11	0.15 ± 0.08
NGC 2345	3044665967836430976	4251 ± 14	1.08 ± 0.04	−0.26	−0.23 ± 0.09
NGC 2345	3044669232011557760	4468 ± 13	1.28 ± 0.05	−0.16	−0.11 ± 0.09
NGC 2358	2934861658580860928	5044 ± 11	2.57 ± 0.02	−0.09	−0.02 ± 0.05
NGC 2358	2934838637556373888	5129 ± 13	2.62 ± 0.03	−0.04	0.03 ± 0.05
NGC 2358	2934834411308570624	5155 ± 11	2.88 ± 0.03	−0.07	0.00 ± 0.04
NGC 7654	2015645057006454144	4001 ± 12	0.18 ± 0.04	−0.38	
NGC 7654	2015663649928489856	6072 ± 16	1.16 ± 0.03	−0.19	−0.05 ± 0.09
Stock 1	2024990807120270976	4996 ± 17	2.58 ± 0.03	0.06	0.15 ± 0.07
Trumpler 2	454676374812927744	4071 ± 7	0.83 ± 0.03	−0.40	−0.34 ± 0.05
Trumpler 2	457691785453711360	4370 ± 8	1.30 ± 0.03	−0.26	−0.19 ± 0.04
UBC 54	233820772674404736	5064 ± 19	2.47 ± 0.03	−0.04	0.05 ± 0.05
UBC 54	233049705784504576	5089 ± 14	2.27 ± 0.04	−0.05	0.01 ± 0.05

Notes. We also list the iron abundances computed with respect to the Sun ([Fe/H]). The stars without abundance values correspond to the two identified supergiants (COIN-Gaia 6 and NGC 7654), and the two stars with low S/N are from COIN-Gaia 6, as discussed in Sect 4.2.

Table B.3. Comparison of the atmospheres parameters determined by different authors.

Star	T_{eff}[K]				$\log g$				[Fe/H]		
	Here	R16	A19	H19	Here	R16	A19	H19	Here	A19	H19
3044665967836430976	4251±14	4300	4183±52	4020	1.08±0.04	1.60	0.96±0.09	1.03	-0.22±0.09	-0.39±0.08	-0.28±0.07
3044669232011557760	4468±13	4300	4283±25	4350	1.28±0.05	1.20	1.06±0.09	1.60	-0.11±0.09	-0.29±0.04	-0.32±0.07

References. (R16) Reddy et al. (2016); (A19) Alonso-Santiago et al. (2019); (H19) Holanda et al. (2019).

Table B.4. Obtained solar abundances.

element	$A(X)$
Al I	6.46 ± 0.01
Ba II	2.16 ± 0.01
Ca I	6.37 ± 0.04
Ce II	1.40 ± 0.01
Co I	4.82 ± 0.03
Cr I	5.60 ± 0.03
Fe I	7.43 ± 0.04
Fe II	7.42 ± 0.05
Mg I	7.52 ± 0.01
Mn I	5.44 ± 0.04
Na I	6.32 ± 0.01
Nd II	1.33 ± 0.01
Ni I	6.18 ± 0.04
Sc II	3.15 ± 0.03
Si I	7.51 ± 0.03
Ti I	4.86 ± 0.04
Ti II	4.88 ± 0.04
V I	3.86 ± 0.03
Y II	2.16 ± 0.01

Table B.5. Average abundances for the observed clusters. We included only a few elements. The CDS version includes all the elements studied.

Cluster	[Mg/H]	[Si/H]	[Ca/H]	[Fe/H]	[Ba/H]	N
ASCC 23	-0.04 ± 0.04	0.14 ± 0.08	0.05 ± 0.07	-0.02 ± 0.06	0.45 ± 0.11	1
Alessi 44	0.00 ± 0.02	0.13 ± 0.05	0.05 ± 0.03	0.04 ± 0.05	0.19 ± 0.09	1
Alessi 62	0.09 ± 0.0	0.12 ± 0.07	0.16 ± 0.02	0.10 ± 0.04	0.31 ± 0.01	2
COIN-Gaia 2	0.01 ± 0.01	0.01 ± 0.01	0.06 ± 0.01	0.04 ± 0.02	0.32 ± 0.11	2

Table B.6. Orbital parameters obtained for the studied clusters

Cluster	r_{apogeo}	$r_{perigeo}$	R_{birth}	eccentricity	z_{max}	phi
ASCC 23	9.48 ± 0.04	7.75 ± 0.09	8.28 ± 0.03	0.1 ± 0.004	0.22 ± 0.01	5.29 ± 2.2
Alessi 44	8.35 ± 0.06	6.82 ± 0.05	8.19 ± 0.12	0.1 ± 0.007	0.11 ± 0.01	5.75 ± 0.04
Alessi 62	9.16 ± 0.04	6.34 ± 0.04	9.04 ± 0.02	0.18 ± 0.001	0.17 ± 0.01	4.74 ± 0.05
COIN-Gaia 2	9.5 ± 0.08	7.8 ± 0.14	8.07 ± 0.22	0.1 ± 0.011	0.14 ± 0.01	1.24 ± 0.12
COIN-Gaia 6	13.35 ± 0.47	10.42 ± 0.14	13.15 ± 0.45	0.12 ± 0.013	0.26 ± 0.04	3.36 ± 0.47
FSR 0951	10.32 ± 0.1	7.79 ± 0.22	9.57 ± 0.09	0.14 ± 0.016	0.17 ± 0.02	5.66 ± 0.57
King 23	10.91 ± 0.25	7.47 ± 0.25	9.03 ± 0.98	0.19 ± 0.012	0.37 ± 0.02	2.46 ± 1.37
NGC 581	9.81 ± 0.08	9.7 ± 0.07	9.7 ± 0.07	0.01 ± 0.001	0.06 ± 0.01	5.88 ± 0.01
NGC 1027	9.58 ± 0.06	7.35 ± 0.18	8.48 ± 0.06	0.13 ± 0.01	0.21 ± 0.01	0.97 ± 0.10
NGC 1647	9.7 ± 0.05	8.01 ± 0.07	8.65 ± 0.07	0.1 ± 0.003	0.18 ± 0.01	2.77 ± 0.05
NGC 1750	9.68 ± 0.05	8.08 ± 0.09	8.48 ± 0.1	0.09 ± 0.004	0.12 ± 0.01	5.85 ± 0.09
NGC 2186	10.31 ± 0.11	8.65 ± 0.1	9.14 ± 0.1	0.09 ± 0.007	0.22 ± 0.01	0.46 ± 0.06
NGC 2281	8.58 ± 0.06	7.26 ± 0.01	8.44 ± 0.04	0.08 ± 0.004	0.18 ± 0.01	0.91 ± 0.04
NGC 2345	10.01 ± 0.11	9.16 ± 0.17	9.39 ± 0.21	0.04 ± 0.005	0.09 ± 0.01	1.28 ± 0.08
NGC 2358	8.86 ± 0.03	7.08 ± 0.06	8.69 ± 0.05	0.11 ± 0.003	0.03 ± 0.01	5.59 ± 0.06
NGC 7654	8.79 ± 0.04	7.69 ± 0.13	7.69 ± 0.12	0.07 ± 0.006	0.06 ± 0.01	2.07 ± 0.08
Stock 1	8.19 ± 0.02	6.5 ± 0.09	7.95 ± 0.13	0.12 ± 0.007	0.06 ± 0.01	5.49 ± 0.05
Trumpler 2	8.54 ± 0.03	8.08 ± 0.05	8.08 ± 0.05	0.03 ± 0.003	0.1 ± 0.01	3.26 ± 0.02
UBC 54	9.02 ± 0.05	7.12 ± 0.05	7.68 ± 0.04	0.12 ± 0.004	0.1 ± 0.01	5.11 ± 0.02